

SIZES OF $\text{Ly}\alpha$ -EMITTING GALAXIES AND THEIR REST-FRAME ULTRAVIOLET COMPONENTS AT $z = 3.1$ ¹

Nicholas A. Bond, Eric Gawiser², Caryl Gronwall, Robin Ciardullo³, Martin Altmann⁴, and
Kevin Schawinski^{5,6}
nbond@physics.rutgers.edu

ABSTRACT

We present a rest-frame ultraviolet analysis of ~ 120 $z \sim 3.1$ Lyman Alpha Emitters (LAEs) in the Extended Chandra Deep Field South (ECDF-S). Using *Hubble Space Telescope* (*HST*) images taken as part of the Galaxy Evolution From Morphology and SEDS (GEMS) survey, Great Observatories Origins Deep Survey (GOODS), and Hubble Ultradeep Field (HUDF) surveys, we analyze the sizes of LAEs, as well as the spatial distribution of their components, which are defined as distinct clumps of UV-continuum emission. We set an upper limit of ~ 1 kpc ($\sim 0''.1$) on the rms offset between the centroids of the continuum and $\text{Ly}\alpha$ emission. The star formation rates of LAE components inferred from the rest-frame ultraviolet continuum range from $\sim 0.1 M_{\odot} \text{ yr}^{-1}$ to $\sim 5 M_{\odot} \text{ yr}^{-1}$. A subsample of LAEs with coverage in multiple surveys (at different imaging depths) suggests that one needs a signal-to-noise ratio, $S/N \gtrsim 30$, in order to make a robust estimate of the half-light radius of an LAE system. The majority of LAEs have observed half-light radii $\lesssim 2$ kpc, and LAE components typically have observed half-light radii $\lesssim 1.5$ kpc ($\lesssim 0''.20$). Although only $\sim 50\%$ of the detected LAE components are resolved at GOODS depth, the brightest ($V \lesssim 26.3$) are all resolved in both GOODS and GEMS. Since we find little evidence for a correlation between the rest-UV sizes and magnitudes of LAEs, the majority should be resolved in a deeper survey at the $\sim 0''.05$ angular resolution of *HST*. Most of the multi-component LAEs identified in shallow frames become connected in deeper images, suggesting that the majority of the rest-UV “clumps” are individual star-forming regions within a single system.

Subject headings: cosmology: observations — galaxies: formation – galaxies: high-redshift – galaxies: structure

²Physics and Astronomy Department, Rutgers University Piscataway, NJ 08854-8019, U.S.A.

³Department of Astronomy and Astrophysics, Pennsylvania State University, University Park, PA 16802, U.S.A.

⁴University of Heidelberg, Center for Astronomy, Mönchhofstr. 12-14, D-69120 Heidelberg, Germany

⁵Department of Physics, Yale University, New Haven, CT 06511, U.S.A.

⁶Yale Center for Astronomy and Astrophysics, Yale University, P.O. Box 208121, New Haven, CT 06520, U.S.A

¹Based on observations made with the NASA/ESA Hubble Space Telescope, and obtained from the Hubble Legacy Archive, which is a collaboration between the Space Telescope Science Institute (STScI/NASA),

1. INTRODUCTION

In the local universe, the majority of galaxies fall on a sequence that runs from red, quiescent galaxies with a compact spheroidal component to star-forming, gas-rich disks with approximately exponential profiles. Out to intermediate redshifts ($z \sim 1.5$), there is a clear continuum in morphological properties that is consis-

the Space Telescope European Coordinating Facility (ST-ECF/ESA) and the Canadian Astronomy Data Centre (CADC/NRC/CSA).

tent with the Hubble Sequence that we observe locally (Conselice et al. 2004). However, at higher redshifts, typical galaxies appear clumpy and irregular (e.g., Steidel et al. 1996; Papovich et al. 2005; Conselice et al. 2005; Venemans et al. 2005; Pirzkal et al. 2007) and evade clean placement into existing classification schemes.

The most studied class of galaxy includes objects found by the Lyman-break technique, wherein high-redshift galaxies are identified by a flux discontinuity in the continuum caused by absorption of intervening neutral hydrogen (Steidel et al. 1996). Morphological analyses of $z > 2.5$ Lyman-break galaxies (LBGs) have revealed that most of these systems are disturbed and disk-like (i.e., with exponential light profiles), with only $\sim 30\%$ having light profiles consistent with galactic spheroids (e.g., Ferguson et al. 2004; Lotz et al. 2006; Ravindranath et al. 2006). In addition, using SExtractor, these studies find a mean half-light radius of ~ 2.27 kpc at $z = 3.1$ and a size evolution that scales approximately as $H^{-1}(z)$.

Like LBGs, Lyman Alpha Emitters (LAEs) at $z \sim 2 - 4$ are widely believed to be actively star-forming (e.g. Cowie & Hu 1998). However, they are found to have lower stellar and dark matter masses, higher mass-specific star-formation rates, and lower dust content on average (Venemans et al. 2005; Gawiser et al. 2007). The effort to measure the morphologies of these objects is still in its earliest stages, with the majority of the existing results being reported in the broadband rest-frame ultraviolet. The qualitative rest-UV morphological properties of LAEs are generally agreed upon, but LAEs remain difficult to place in existing classification schemes. At $3 \lesssim z \lesssim 6$, most are small (with half-light radii $\lesssim 1$ kpc), compact ($C > 2.5$), and barely resolved at *Hubble Space Telescope* (*HST*) resolution (Venemans et al. 2005; Pirzkal et al. 2007; Overzier et al. 2008; Taniguchi et al. 2009). However, many ($\sim 20 - 45\%$) are clumpy or irregular, with components extending to several kiloparsecs.

The Multiwavelength Survey by Yale-Chile (MUSYC, Gawiser et al. 2006) is a collaborative effort to obtain multiwavelength imaging and spectroscopy of 1.2 degree² of sky in four different fields, including the Extended Chandra Deep Field-South (ECDF-S). As part of this survey,

Gronwall et al. (2007) used broadband and 4990 \AA narrow-band imaging of the ECDF-S to identify a large, unbiased sample of LAEs at $z = 3.1$. The authors found that their LAE sample had an exponential equivalent width distribution, with a scale length of $w_0 = 76_{-8}^{+11}$, and followed a Schechter function (Schechter 1976) in emission-line luminosity, with $\alpha = -1.49_{-0.34}^{+0.45}$ and $\log L^* = 42.64_{-0.15}^{+0.26}$. In addition, they found that the star formation rates (SFRs) estimated from the UV continuum were ~ 3 times larger than those estimated from the Ly α line, with UV SFRs ranging from ~ 1 to $10 M_{\odot} \text{ yr}^{-1}$. Subsequent analysis of this sample by Gawiser et al. (2007) showed LAEs to be weakly clustered, with a bias factor ($b \sim 1.7$) consistent with that expected from the progenitors of present-day L^* galaxies. Moreover, although $\sim 70\%$ of these LAEs are too faint to be detected on deep images taken by the *Spitzer* Infrared Array Camera, spectral energy distribution fits to the broadband optical and infrared colors of a mean “stacked” LAE suggests that they typically have very small stellar masses, $\sim 10^9 M_{\odot}$.

This paper complements the Gronwall et al. (2007) and Gawiser et al. (2007) studies of the MUSYC $z = 3.1$ LAE sample by measuring the rest-UV size and component distributions using high-resolution V -band images, taken by the Advanced Camera for Surveys (ACS) and obtained as part of the Galaxy Evolution from Morphology and SEDs survey (GEMS, Rix et al. 2004), Great Observatories Origins Deep Survey (GOODS, Giavalisco et al. 2004), and Hubble Ultradeep Field survey (HUDF, Beckwith et al. 2006). In addition to presenting the largest LAE morphological study to date, this paper describes a new pipeline for the study of high-redshift galaxies at low signal-to-noise. In past work, clumpy LAEs have been given only crude, qualitative descriptions, but even at low redshift, ordinary late-type galaxies can look clumpy in the UV. Thus, there is ambiguity in the treatment of individual components (Bond 2009, and references therein). Here, we fit each photometric component separately and give quantitative size measures for both the individual components *and* the LAE system as a whole. Furthermore, since some of our LAEs are covered in multiple surveys, we present an analysis of the depth dependence of the sizes and compo-

ment distributions. As discussed in Bond (2009), this is a crucial step if we wish to compare morphological measurements between different high-resolution imaging observations of LAEs. We will present an analysis of the higher-order morphological properties of LAE components in a subsequent paper (C. Gronwall et al. 2009, in preparation).

In § 2 and 3, we describe the data and detail the pipeline used in our analysis. In § 4, we present the photometric properties, including half-light radii, of each LAE system and its components. We also explore how these properties vary with image depth. Finally, in § 5, we discuss the implications of our findings and suggest a direction for future morphology studies of LAEs and other high-redshift galaxies. Throughout this paper, we will assume a concordance cosmology with $H_0 = 71 \text{ km s}^{-1} \text{ Mpc}^{-1}$, $\Omega_m = 0.27$, and $\Omega_\Lambda = 0.73$ (Spergel et al. 2007). With these values, $1'' = 7.75 \text{ physical kpc}$ at $z = 3.1$.

2. DATA

Our study uses the statistically complete sample of $z = 3.1$ LAEs identified by Gronwall et al. (2007) in the Extended Chandra Deep Field-South; these objects are defined to have monochromatic fluxes, $F_{4990} > 1.5 \times 10^{-17} \text{ ergs cm}^{-2} \text{ s}^{-1}$, and observed-frame Ly α equivalent widths, $EW > 80 \text{ \AA}$. As published, the Gronwall et al. (2007) sample contains 162 objects. From this list, we exclude the two X-ray sources removed by the authors, one duplicate object (LAE 110, identical to LAE 124), and five recently-identified spurious detections (LAEs 33, 48, 57, 104, and 139, Guillermo Blanc, private communication) caused by CCD cross-talk in the narrow-band image. Excluding LAEs within 40 pixels of the edge of an image, a total of 116 of the remaining 154 objects fall in fields observed by *HST*; these are listed in Table 1. Below, we summarize the data.

2.1. GEMS

The GEMS survey consists of a series of 63 ACS pointings in the V_{606} and z_{814} -bands, which cover the full $\sim 800 \text{ arcmin}^2$ of the ECDF-S. The depth of this survey is fairly uniform across the field, with V_{606} -band point sources detected with 5σ confidence to $m_{\text{AB}} = 28.3$ in the main GEMS survey, and to $m_{\text{AB}} = 27.9$ in the region cov-

ered by the first epoch of the GOODS survey (hereafter, sGOODS). The sGOODS data were reduced with the GEMS pipeline, but include data incorporated into the deeper GOODS *v2.0* images and will therefore only be used to test the depth dependence of our morphological diagnostics (see § 3.4). All images have been multidrizzled (Koekemoer et al. 2002) to a pixel scale of $0''.03 \text{ pixel}^{-1}$ and in the GEMS-only tiles, 97/154 LAEs are covered by the survey.

2.2. GOODS

In the Chandra Deep Field-South, the southern half of the GOODS survey covers $\sim 160 \text{ arcmin}^2$ of sky and includes *HST*/ACS observations in the B_{435} , V_{606} , I_{775} , and z_{850} filters. The effective exposure time of this survey is variable across the GOODS area, but for point sources, a typical V_{606} -band, 5σ detection limit is $m_{\text{AB}} = 28.8$. All images have been multidrizzled to a pixel scale of $0''.03 \text{ pixel}^{-1}$ and of 154 LAEs in our original sample, 29 have V_{606} -band coverage in *v2.0* of the GOODS/ACS catalog.

2.3. HUDF

The images of the Hubble Ultra-Deep Field (HUDF) are deeper than those in either GEMS or GOODS, reaching V -band 5σ point source depth of $m_{\text{AB}} = 30.5$, but cover only 11 arcmin^2 of sky. As in GOODS, the HUDF survey includes *HST*/ACS observations in the B_{435} , V_{606} , I_{775} , and z_{850} filters, which have been multidrizzled to a plate scale of $0''.03 \text{ pixel}^{-1}$. Only 3 of our 154 objects fall in this region.

3. METHODOLOGY

High-redshift galaxies frequently exhibit “clumpy” morphologies; in such systems, high-order morphological fits can be difficult to interpret. To avoid this problem, each LAE system was first examined with SExtractor (Bertin & Arnouts 1996), to identify individual rest-UV components. The pipeline developed for this work operated in five stages:

- Cutout extraction from survey images (§ 3.1)
- Source detection, using SExtractor (§ 3.1)

TABLE 1
HST IMAGING SURVEY PROPERTIES

Survey	Sky Coverage (arcmin ²)	V-band Depth ^a (AB mags)	$N_{\text{LAE}}^{\text{b}}$	Reference
GEMS	800	28.3 ^c	97	1
GOODS	160	28.8	29	2
HUDF	11	30.5	4	3

^a5 σ depth for point source detection

^bNumber of LAEs covered in the survey region

^cThe sGOODS data are shallower, 27.9 AB mags

References. — (1) Rix et al. 2004; (2) Giavalisco et al. 2004; (3) Beckwith et al. 2006

- Centroid estimation and aperture photometry using PHOT (§ 3.2)
- Light profile fitting, using GALFIT (§ 3.3)
- Identification of point sources (§ 3.3)

3.1. Cutouts and SExtractor Runs

We began by extracting an 80×80 pixel ($2''.4 \times 2''.4$) cutout from the *HST*/ACS survey image at the position of each LAE in our sample. This region, which has a linear scale of ~ 19 kpc at the redshift of the emitter, is large enough to include the expected uncertainties in the V-band centroids (see § 3.2). Since the profile fits described in § 3.3 were performed over the entire cutout, our final sample included only those LAEs with full survey coverage in the cutout region.

After extracting the cutouts, we identified all sources contained within them using the SExtractor (Bertin & Arnouts 1996) object detection algorithm. Since LAEs can appear as either point sources or extended objects at *HST* resolution, we set our parameters to find all sources with at least nine pixels above a 1.65σ detection threshold. Although this condition does not allow us to find very weak compact sources, even when they are apparent to the eye, this limitation is not serious, since these objects contain no useful morphological information. Finally, to identify those objects with

multiple components, we set the SExtractor parameter, DEBLEND_MINCONT= 0.06; this value was chosen to split the LAE components which appeared by eye to be separate objects.

Figure 1 plots the distribution of SExtractor V₆₀₆-band detections in the 97 GEMS cutouts as a function of angular distance from the ground-based Ly α centroid. The detections are highly clustered: 34 components fall within $0''.25$ of the ground-based position, which is the approximate positional uncertainty associated with the ground-based astrometry (Gawiser et al. 2006). Moreover, the density of detected components does not fall to that of the field until $\sim 0''.6$, which we define as our selection radius, R_{sel} . Based on the density of field sources displayed in Figure 1, we estimate that 11 of the 87 components detected by SExtractor within our selection radius are chance coincidences.

After discarding those cutouts with no detections within the selection radius, we used SExtractor to fit and subtract a uniform sky from each of the remaining images. This is a critical step; as a result of resonant scattering, the diffuse emission from Ly α can extend many half-light radii beyond the main body of a galaxy (Ostlin et al. 2008). By using a field cutout size of $2''.4$, we minimize the risk that our estimate of the sky will be affected by diffuse emission that may occur within

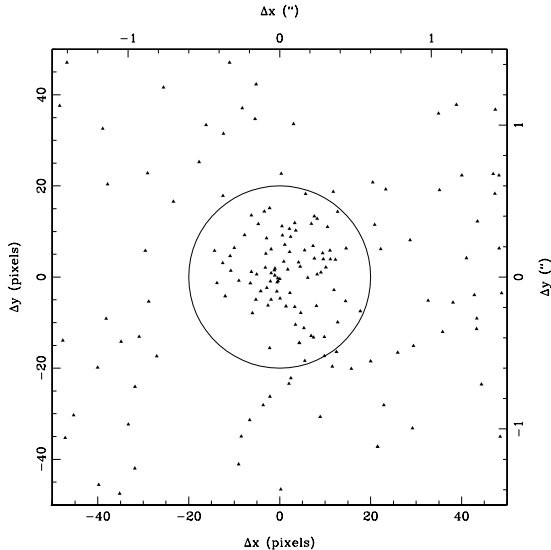


Fig. 1.— Distribution of SExtractor detections in the V_{606} -band GEMS cutouts as a function of distance from the ground-based $\text{Ly}\alpha$ centroid. Within the $0''.6$ (20-pixel) selection radius, drawn in black, are objects classified as LAE components.

our $0''.6$ selection radius. Similarly, by adopting a uniform sky background, we avoid the risk of confusing $\text{Ly}\alpha$ emission with background fluctuations.

3.2. Centroid Estimation and Aperture Photometry

The above procedure is useful for isolating individual components within the LAE cutouts, but we also wish to measure the photometric properties of the composite system; that is, of all light within the selection radius of an LAE. To estimate the rest-UV centroid of the LAE system, we again run SExtractor on each of the cutouts, now requiring a detection to have only five pixels above the 1.65σ threshold. We then measure the centroid to be the flux-weighted mean position of the detections within the selection radius. The smaller five-pixel detection threshold will find more dim components that, although too dim for a reliable half-light radius determination, could allow for a more accurate determination of the LAE centroid.

We then use the IRAF routine PHOT, summing the counts within a series of apertures, each cen-

tered on the measured light centroid and ranging from $0''.015$ – $0''.6$ in radius. Assuming that all of the flux from the LAE system is contained within a $0''.6$ aperture, the half-light radius, r_e^{PHOT} , is found by interpolating the curve of growth at one-half of this total flux. We use a $0''.6$ maximum aperture because it corresponds to the selection radius (larger maximum apertures yield half-light radii that differ by no more than 10%).

3.3. Morphology Fits and Point Source Identification

We measured the morphological properties (presented in detail in Paper 2) of our LAE sample using GALFIT (Peng et al. 2002), a software package that convolves a model light profile with the point spread function (PSF) and minimizes χ^2 over a chosen set of model parameters. GALFIT is fast and capable of simultaneously fitting multiple sources in a given image, making it an efficient option for analyzing large samples of multi-component objects.

For the GEMS and GOODS data, we defined the PSFs using a sample of bright stars located throughout the ECDF-S. Only those stars with centroids lying near the center of a pixel and with peak fluxes well below saturation were used in this definition. In the case of the extremely small field of the HUDF, only a single star was used for the PSF. However, since all three LAEs located in the HUDF are well resolved, this limitation is not important for our study. We then simultaneously fit Sérsic profiles (Sérsic 1968) to all detections within each cutout using elliptical model isophotes. Unless otherwise specified, we fit to the entire cutout, but only report the properties of a component if its center falls within the LAE selection circle. No bad pixel masks were used, and each fit was inspected by eye.

The majority of LAEs have half-light radii < 1 kpc in V_{606} (Venemans et al. 2005; Pirzkal et al. 2007; Overzier et al. 2008), so many of the objects in our sample may be unresolved at the $0''.06$ (~ 0.5 kpc at $z = 3.1$) resolution typical of *HST*. To determine whether an object is resolved, we compare the χ^2 value of its Sérsic fit to that of a fit to the PSF alone; in other words, we require

$$F \equiv \frac{(\chi_{\text{psf}}^2 - \chi_{\text{seraic}}^2)}{\chi_{\text{seraic}}^2} > F_{\text{crit}}. \quad (1)$$

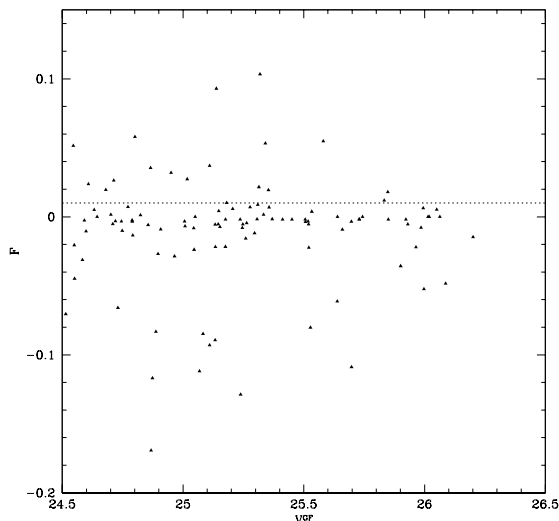


Fig. 2.— Relative improvement of a Sérsic fit vs. a PSF fit (represented by F -values) for 115 known point sources (stars), plotted as a function of the V-band magnitude output by GALFIT. Here, $\sim 85\%$ of true point sources have $F < 0.01 \equiv F_{\text{crit}}$ (indicated by the dashed line).

When data are uncorrelated and have only gaussian random errors, F_{crit} is determined from the F-distribution. Unfortunately, for point sources, the χ^2 surfaces of the Sérsic profile are not well behaved, and GALFIT (which employs the Levenberg-Marquardt algorithm, see Press et al. (1992)) does not always converge to the absolute minimum in χ^2 . Consequently, to perform this test, we computed F_{crit} empirically using known stars.

A sample of high-confidence point sources was obtained from Altmann et al. (2006), who used broadband spectral energy distribution fits to distinguish stars from galaxies in the ECDF-S. From this sample, we selected 912 stars that fall within the GEMS region and had temperatures, $T < 4500$ K, a regime in which photometric confusion with galaxies is minimal. After running SExtractor on the GEMS cutout of each star, we further restricted our sample to 115 objects that were isolated (i.e., the only object in the cutout), well-centered (within $0''.45$ of the cutout center), unambiguously stellar (SExtractor stellarity > 0.9), and faint ($V_{606}^{\text{SE}} > 24.6$). This ensured that we had a

clean sample of stars with photometric uncertainties dominated by sky noise. Finally, we fit our stellar sample to both the point spread function and a Sérsic profile and plot the resulting F values against V-band magnitude (Figure 2). From this plot, we infer that 85% of true point sources will have $F < 0.01 \equiv F_{\text{crit}}$ (indicated by the dashed line); we use this threshold to identify LAE components that are consistent with point sources.

3.4. Objects with Coverage in Multiple Surveys

Many of the standard measures of a galaxy’s morphology exhibit a systematic offset from their intrinsic values if measured on low signal-to-noise (S/N) images. For example, Ravindranath et al. (2006) have fit Sérsic profiles to a series of model images with a range of S/N. At low signal levels, they see a systematic offset between the input and output Sérsic index, n , where it is overestimated for model disks and underestimated for model spheroids.

Since there are regions of overlap in the sky coverage of the HUDF, GOODS, and GEMS surveys, we can estimate this dependence using a subsample of LAEs in the field. Specifically, since the HUDF is a subregion of the GOODS survey, all three of the LAEs in that field also have GOODS and sGOODS data. Similarly, 22/29 LAEs in GOODS are also present in sGOODS, and there is a small region of overlap between GOODS and GEMS which contains nine LAEs. We note that there is a systematic offset between the world coordinate systems (WCS) of the GOODS and sGOODS images in the northern part of the Chandra Deep Field-South. A comparison of the positions of bright sources in each survey shows that the coordinates from GOODS must be shifted by -7 pixels in x and -7.2 pixels in y to match the sGOODS WCS. Astrometric consistency between surveys is critical for us to accurately match individual LAE components.

4. RESULTS

4.1. Fixed Aperture Half-Light Radii

Table 2 contains the PHOT-derived $0''.6$ -aperture magnitudes (V^{PHOT}) and half-light radii (r_e^{PHOT}) for all LAEs in the *HST* surveys. In GEMS, six of

the 97 objects have no counterpart in the $0''.6$ selection radius, while another six have no detected components, but do have $0''.6$ aperture fluxes at $> 2\sigma$ level ($V^{\text{PHOT}} < 28.45$). In GOODS, only one object (LAE 84) has an aperture flux $< 2\sigma$, but another five have no SExtractor detections. All three of the HUDF LAEs have SExtractor detections within $0''.6$. Among the LAEs for which we could determine a centroid, there is no evidence for an offset between the Ly α emission and that of the continuum. The best-fit two-dimensional gaussian to the distribution of these offsets has $\sigma = 0''.21$, which is consistent with the expected $\sim 0''.2 - 0''.3$ astrometric uncertainties of the ground-based observations (Gawiser et al. 2006).

Figure 3 displays a histogram of the *observed* half-light radii for the LAEs in the GEMS (solid), GOODS (dotted), and HUDF (one for each arrow) surveys. There is a clear excess of sources near the ~ 0.6 kpc resolution limit of GEMS and GOODS, suggesting that a typical LAE is either unresolved or only barely resolved at *HST* resolution. The mean half-light radii of the detected LAEs are $\bar{r}_e^{\text{PHOT}} = 0.98$ kpc, 0.91 kpc, and 1.53 kpc in GEMS, GOODS, and HUDF, respectively. For comparison, Overzier et al. (2008) give $\bar{r}_e^{\text{PHOT}} = 0.9$ kpc as the mean rest-frame UV half-light radii of 12 LAEs at $z = 4.1$.

Figure 4 plots the dependence of r_e^{PHOT} with V^{PHOT} . The GEMS data show little correlation between the two parameters, but the deeper GOODS data display weak evidence for an increase in size with increasing flux. There is also little evidence for a correlation between the continuum half-light radius, r_e^{PHOT} , and Ly α equivalent width (EW(Ly α), see Figure 5). The EW(Ly α) values are estimated in Gronwall et al. (2007) using the broadband and narrow-band photometry. We plot only LAEs with $S/N > 30$ in Figure 5 (not that little correlation is seen even when the entire sample is plotted).

Our curve-of-growth measurement of r_e^{PHOT} is model-independent; thus, if the rest-UV LAE centroids are well determined, r_e^{PHOT} should be insensitive to the depth of the survey. However, if the rest-UV continuum is diffuse or clumpy, the SExtractor detections, and therefore the derived centroids and r_e^{PHOT} may vary with depth. In fact, there is clear evidence for this in Figure 6,

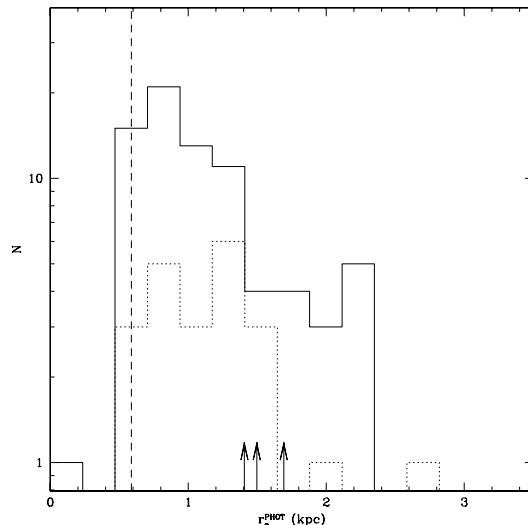


Fig. 3.— Distributions of fixed-aperture, observed half-light radii for objects in GEMS (solid curve), GOODS (dotted), and HUDF (one for each arrow). The dashed line is the approximate resolution limit of the V-band *HST* images.

which plots the fractional difference in r_e^{PHOT} between surveys as a function of V-band magnitude. At magnitudes brighter than $V^{\text{PHOT}} \sim 26.3$ ($S/N \gtrsim 30$ in GEMS), the half-light radius is robust to $< 10\%$ in all surveys. However, only the HUDF-GOODS comparison fares well between $26 < V^{\text{PHOT}} < 27$, and at fainter magnitudes, there is evidence that the shallower surveys are systematically overestimating the half-light radius. Over the entire magnitude range, the variance of $\Delta r_e^{\text{PHOT}}/r_e^{\text{PHOT}}$ between GOODS and sGOODS is $\sim 20\%$. GEMS is deeper than sGOODS, so if we assume that the GOODS morphological parameters are accurate, then this would be a conservative estimate of the average error in r_e^{PHOT} in the GEMS data.

4.2. SExtractor Results

Of the 97 LAEs covered by the GEMS survey, 76 have at least one component detected within the $0''.6$ selection circle, 16 have at least two components, and 4 have at least three components. For comparison, Taniguchi et al. (2009) find only 2/47 multi-component LAEs at $z = 5.7$. While

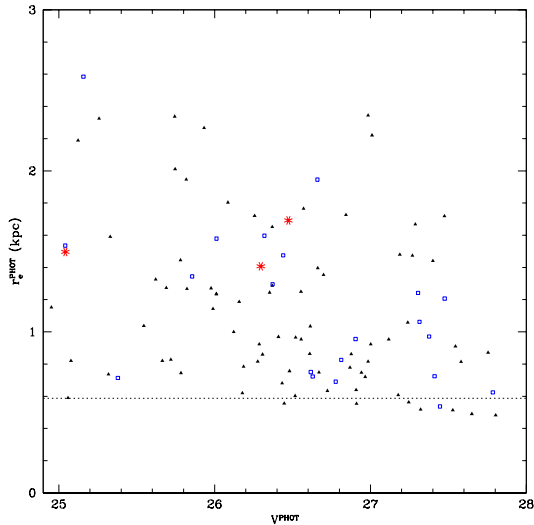


Fig. 4.— Fixed-aperture, rest-UV half-light radius plotted versus rest-UV continuum magnitude in the full sample of LAEs with SExtractor detections, including objects in GEMS (black triangles), GOODS (blue open squares), and HUDF (red asterisks). The dotted line indicates the approximate resolution limit of the V-band *HST* images.

it is tempting to interpret this as evolution in the number of components, the *HST* images used by Taniguchi et al. (2009) are effectively 2.5 magnitudes shallower than even GEMS, and inspection of our images implies that very few LAEs would be seen to have multiple components at that depth.

The cutouts for all LAEs in GEMS are plotted in Figure 10, with the components marked by red arrows and the selection circle shown in black. Of the objects with multiple components, eight appear to have a clumpy morphology and may correspond to merging galaxies or individual star-forming clumps in a single galaxy. The remaining eight cutouts have one cleanly defined detection, and “fuzz” that appears just above the noise or as an extension to the primary source. We note that, based on the field density of objects, we expect ~ 11 of the components detected by SExtractor to be unrelated to observed Ly α emission (see § 3.1). Hence, several of the apparently clumpy or fuzzy objects shown here may be interlopers.

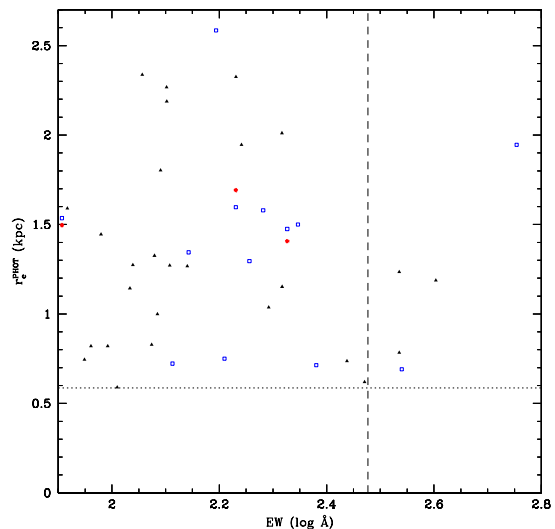


Fig. 5.— Fixed-aperture, rest-UV half-light radius plotted as a function of Ly α equivalent width, where EW(Ly α) measurements are taken from Gronwall et al. (2007). LAEs with S/N > 30 in the V-band images are plotted, including objects in GEMS (black triangles), GOODS (blue open squares), and HUDF (red asterisks). The dotted line indicates the approximate resolution limit and the dashed line indicates the approximate EW(Ly α) at which Ly α emission is 50% of the light detected in the V-band filter.

In Figure 11, we plot the 29 LAEs covered by the GOODS survey. Of these, 23 have at least one component, four have two components, and one (LAE 4) has five components. The ground-based narrow-band magnitude of LAE 4 is the second brightest of the LAEs in our full sample of 155 objects, so its complex and extended morphology may suggest a protocluster or a massive galaxy in the act of formation. The rightmost of the two components in LAE 11 may be an interloper (we expect ~ 3 contaminants in the GOODS components sample) due to its large extent and position on the edge of the selection circle. Of the remaining three multi-component objects, LAE 25 and LAE 44 appear to be clumpy and LAE 55 is noisy and may be a single extended object. Several of the single-component LAEs, such as LAE 56, 59, and 125, have asymmetric diffuse emission about the emission centroid; while this is consistent with

possible merger activity, it could also be caused by an asymmetric distribution of diffuse star formation or dust. Finally, in Figure 12, we plot cutouts for the three LAEs with HUDF coverage. All are detected as a single component within the selection circle and all show evidence for asymmetric, extended emission in both GOODS and HUDF. It is worth noting that these three objects are not necessarily representative of the overall LAE population; that is, none of the point-like or faint LAEs seen in GOODS are covered by HUDF.

The position, brightness, ellipticity, positional angle and observed half-light radius (r_e^{SE}) of each LAE component (as computed by SExtractor) are given in Table 3. In addition, the r_e^{SE} distributions are given in Figure 7. The mean r_e^{SE} of the entire sample of LAE components is 0.74 kpc in GEMS (0.79 kpc in GOODS), while for sources with only one SExtractor detection (i.e., non-clumpy sources) the mean is 0.73 kpc in GEMS (0.67 kpc in GOODS). This is somewhat smaller than the median size of $r_h \sim 1$ kpc found for non-clumpy $z = 3.1$ LAEs by Venemans et al. (2005), but their decision to include only sources with 15 connected pixels above a 1σ threshold would have made them insensitive to some of the smaller and fainter objects found in our sample. Considering this difference in selection criteria, as well as the small number of objects involved (they computed the median half-light radius using only 13 objects), the two results are probably consistent. In HUDF, all three of the LAEs have a single SExtractor detection within $0''.6$, with $\bar{r}_e^{\text{SE}} = 1.47$ kpc. Although these deeper observations may be picking up diffuse emission that is increasing the mean half-light radius, the sample is too small to draw strong conclusions.

The ability of SExtractor to detect LAE components will clearly depend on survey depth, with the faintest objects likely to go undetected in the shallowest exposures. As expected, the fraction of LAEs with no counterpart in the *HST* images decreases with depth, with 27% (6/22) in sGOODS, 22% (21/97) in GEMS, 20% (6/29) in GOODS, and 0% (0/3) in HUDF. Moreover, of the six LAEs not detected in sGOODS, three are present in the full GOODS survey, but all are faint and indistinguishable from point sources (see below). Finally, we note that in the shallow surveys diffuse emission can go undetected below the sky noise,

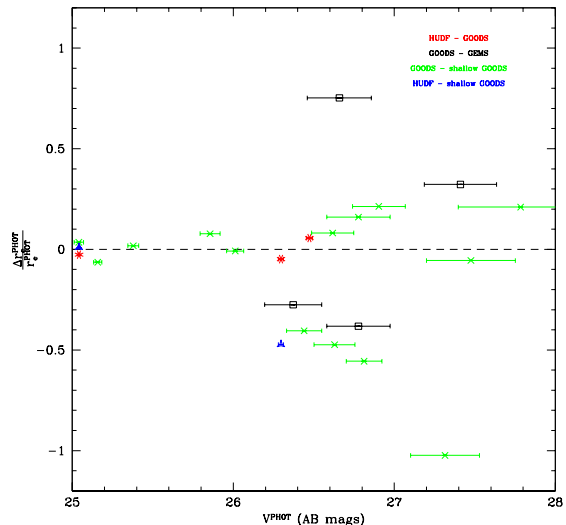


Fig. 6.— Fractional difference in estimates of the fixed-aperture half-light radii for the same objects between different surveys, plotted as a function of V-band magnitude. For all points, Δr_e^{PHOT} indicates the difference between the radius of the deeper minus that of the shallower survey, where green crosses are GOODS vs. shallow GOODS, black open squares are GOODS vs. GEMS, blue triangles are HUDF vs. shallow GOODS, and red asterisks are HUDF vs. GOODS. Fixed-aperture measurements of the half-light radius appear consistent at $V^{\text{PHOT}} \lesssim 26.3$, or $S/N \gtrsim 30$ in GEMS.

and a source with a single component in deeper images can be split into multiple components in shallower ones. This occurs in two of the LAEs (LAE 11 and LAE 125) in the sGOODS survey, but in both cases the vast majority of the total flux is contained in one component.

For our chosen set of parameters, SExtractor performs AUTO photometry within an elliptical aperture with radius $2.5R_{\text{Kron}}$ (Kron 1980), in which R_{Kron} is the first-order moment of the light distribution. The parameter, R_{Kron} , is in turn dependent on the radius at which the source flux drops below the noise. Since this latter quantity is depth-dependent, we expect SExtractor to underestimate the half-light radii of faint sources, particularly those with diffuse emission. In Figure 8, we plot the fractional difference between the

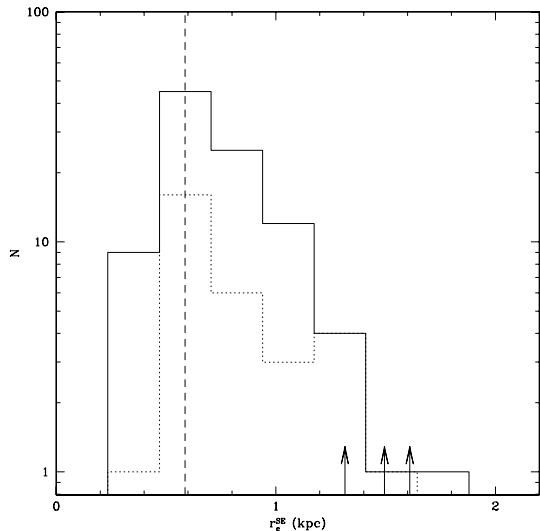


Fig. 7.— Distributions of observed half-light radii, as measured by SExtractor, for LAE components in GEMS (solid curve), GOODS (dotted), and HUDF (one object for each arrow). The dashed line is the approximate resolution limit of the V-band *HST* images.

PHOT half-light radii (computed using our curve-of-growth analysis; see § 3.2) and the SExtractor half-light radii for LAEs with only one detected component. For LAEs in GEMS with $S/N \gtrsim 30$ ($V^{\text{SE}} \lesssim 26.3$), the two radii agree to $\sim 10\%$, but then they diverge rapidly at fainter magnitudes. The same is true for LAEs in the GOODS survey, where $S/N \gtrsim 30$ corresponds to $V^{\text{SE}} \lesssim 26.8$. We don’t have enough objects in HUDF to determine the flux at which the two radii diverge, but the half-light radius measurements appear consistent in the three $V^{\text{SE}} > 26.6$ LAEs present in the survey.

4.3. Point Source Samples

Figure 9 plots the distribution of F (see Equation (1)) as a function of the best-fit V-band magnitude calculated by GALFIT (V^{GF}). LAE components imaged in the GEMS and GOODS surveys (shown as black triangles and blue open squares, respectively) are consistently resolved at $V^{\text{GF}} \lesssim 26.5$ and consistently unresolved at $V^{\text{GF}} \gtrsim 27$. That the dimmest components are consistent with

a point source is simply a reflection of the fact that objects barely detected above the sky noise can be fit just as well with a three-parameter PSF as with the seven-parameter Sérsic profile. There are three anomalous components in the GOODS sample at $V^{\text{GF}} \sim 27.5$, all of which are members of the morphologically complex system, LAE 5, and appear inconsistent with point sources despite their faint magnitudes.

It is important to note that not all of the “point source” LAEs are isolated. In the GEMS sample, only 20 of the 45 unresolved sources had no other object within the selection circle. Of the remaining 25 components, 12 appear to be part of a multi-component source, and 13 appear to the eye to be extensions of a larger, amorphous object that was split by SExtractor. As discussed in § 3.1, we expect ~ 11 contaminants in our sample, so some of these components must be chance superpositions and not associated with the Ly α emission. In GOODS, a larger fraction (70%) of the 23 unresolved sources are isolated, perhaps due to the decreased tendency for LAEs to be split into multiple components (see 4.2).

Since the brightest LAE components are all resolved, it is possible that a deeper survey would resolve many of the apparent point sources. Indeed, the fraction of unresolved LAE components drops from 63% (12/17) in sGOODS to 47% (45/95) in GEMS and 48% (15/31) in the full GOODS survey. Moreover, only four of the 12 point sources in sGOODS remain unresolved at GOODS depth. In the HUDF, only one of the three sources is consistent with a point source, and it appears as an extension to a brighter, resolved component.

5. DISCUSSION

5.1. Optimal Techniques for LAE Morphological Analysis

When analyzing the morphologies of LAEs, there is a great deal of ambiguity as to how one should treat objects with multiple clumps. Some components may be the result of merging/interacting galaxies; others may simply be individual star-formation regions within a single system. In this paper, we have considered both possibilities, presenting magnitudes and half-light radii both for the LAE system as a whole (using fixed apertures about the light centroid) and for indi-

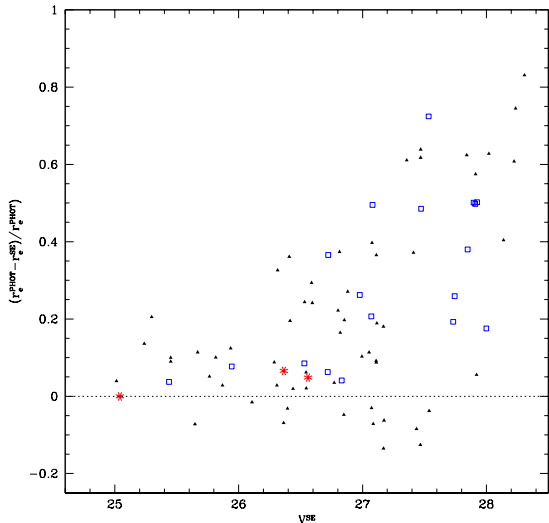


Fig. 8.— Fractional difference between the fixed-aperture half-light radii (computed within $0''.6$ apertures) and the SEExtractor half-light radii for LAEs with only one detected component, plotted as a function of the rest-UV continuum magnitude computed by SEExtractor. Objects in GEMS are plotted as black triangles, objects in GOODS as blue open squares, and objects in HUDF as red asterisks. The two measures of observed half-light radius appear consistent with one another at $V^{\text{PHOT}} \lesssim 26.3$, or $S/N \gtrsim 30$ in GEMS and GOODS. The dotted line marks $r_e^{\text{PHOT}} - r_e^{\text{SE}} = 0$.

vidual LAE components. We find that the majority of multi-component LAEs identified in shallow frames become connected on deeper images. This suggests that the majority of rest-UV “clumps” are actually individual star-forming regions within a single system.

The presence of this diffuse emission connecting individual clumps suggests that, in the absence of interlopers, LAE radii and total magnitudes should be determined using fixed aperture measurements. SEExtractor-like adaptive techniques that rely on isophotal radii will tend to underestimate an LAE’s true half-light radius since they only consider the extended emission surrounding the brightest clumps (see Figure 6). The distinction between definitions of half-light radius is particularly important when comparing

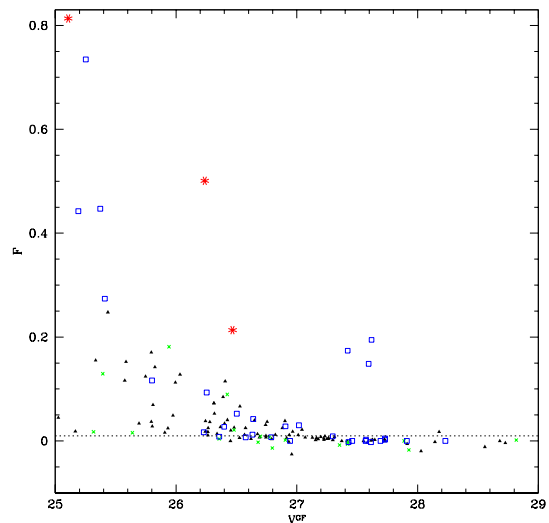


Fig. 9.— Distribution of F (see Equation 1) values as a function of the SEExtractor V-band magnitude for LAE components in GEMS (black triangles), GOODS (blue open squares), shallow GOODS (green crosses), and HUDF (red asterisks). We mark with a dotted line $F = F_{\text{crit}} = 0.01$ – all of the LAE components appear to be above this line (and therefore, resolved) at $V^{\text{PHOT}} \lesssim 26.3$, or $S/N \gtrsim 30$ in GEMS.

the half-light radii of LAEs to those of the more extended Lyman Alpha Blobs (hereafter, LABs, Fynbo et al. 1999; Steidel et al. 2000), which exhibit a wide range of Ly α morphologies and may be the precursors to present-day rich-cluster galaxies (Yang et al. 2009). Similarly, higher-order non-parametric morphological diagnostics, such as CAS (concentration, asymmetry, and clumpiness, Conselice 2003) or the Gini coefficient, should also be performed within a fixed aperture, and not be tied to isophotal radii. Conversely, parametric profile fits that do not account for a clumpy light distribution are best performed on individual components, as these are more closely approximated by a smooth light distribution.

An additional concern involves the reliability of morphological analyses in different signal-to-noise regimes. Figures 4, 6, and 9 suggest that one needs a S/N of at least ~ 30 in the compact core of the LAE in order to resolve the rest-UV continuum

and to make a reasonable estimate of its half-light radius. For the fixed-aperture measurements, the primary limitation is finding the LAE system centroid; for isophotal measurements, it is image classification, and whether the separate components on shallow frames are actually brighter knots of a larger object.

5.2. LAE Sizes and Morphologies

The results presented in § 4 suggest that LAEs at $z \sim 3$ are generally $\lesssim 2$ kpc in size in the rest-frame UV, while the individual components of an LAE system are typically $\lesssim 1.5$ kpc. Both of these results are consistent with previous work. Gawiser et al. (2007) has shown that the majority of LAEs are likely to be in the early phases of a starburst, perhaps even experiencing their first large-scale burst of star-formation. Consequently, we don't expect their sizes or morphologies to vary greatly with wavelength. Even the more massive, and presumably older, LBGs have been shown to have a negligible morphological k -correction between the observed-frame optical and near-infrared (Dickinson 2000). However, we should *not* use the rest-UV morphology to infer the extent and distribution of the Ly α emission. At $z = 3.1$, the V-band probes the rest-UV continuum light from star-forming regions associated with the host galaxy of the LAE. At low redshift, most of the Ly α emission originates in a diffuse halo surrounding the galaxy (Ostlin et al. 2008). Presumably, this is a consequence of resonant scattering in the Ly α line; if the same process occurs at high redshift, then an LAE's Ly α -emission-line morphology will be "smeared" relative to the distribution of its star-forming regions.

If there were extended Ly α halos in a large fraction of LAEs, we might expect to see a correlation between the V-band half-light radius and the equivalent width of the Ly α line due to the increased contribution of the extended Ly α emission to the V-band flux. However, this effect would only begin to appear at $\text{EW}(\text{Ly}\alpha) \gtrsim 300\text{\AA}$ (marked by a dashed line in Figure 5), above which $\gtrsim 50\%$ of the V-band light comes from the emission line. There are only five objects in our sample that meet this criterion and, given the range of half-light radii seen at smaller $\text{EW}(\text{Ly}\alpha)$, it is impossible to say anything about the existence or extent of Ly α halos from this sample alone.

A more direct method of searching for Ly α halos would be to observe LAEs at high resolution in a narrow-band filter. There are currently no published studies of LAE morphologies in Ly α emission, but one is in progress for a subset of the current MUSYC sample (Gronwall 2009, in preparation). Preliminary results from an ACS narrow-band survey of LAEs (Bram Venemans, private communication) suggest that high- z LAEs do indeed have Ly α halos, as the Ly α emission detected in high-resolution images often cannot account for all the flux seen from the ground. Moreover, even in ground-based images, there is evidence that $z \sim 2$ LAEs are more extended in the emission line than in the continuum (Nilsson et al. 2009).

5.3. Star Formation in LAEs

As shown in Gawiser et al. (2007), very few of the LAEs in our sample are detected at X-Ray wavelengths and there is no evidence for high-ionization emission lines in the rest-UV spectra of the remaining objects for which we have spectral information. This suggests that AGN are unlikely to be the power source for the Ly α emission. Although a low-luminosity or obscured AGN may be present in some of these sources (Finkelstein et al. 2009), the fact that the rest-UV light distribution is consistently resolved at $S/N \gtrsim 30$ (see Figure 9) suggests that any ionizing flux is likely coming from massive stars rather than a nuclear source. In addition, the correlation between UV- and Ly α -based estimates of the star formation rate seen in Gronwall et al. (2007) suggests that shock ionization is also not a substantial source of power for the line emission.

In the last column of Table 3, we give the SFRs for individual LAE components, estimated using their rest-frame UV flux (given by V^{SE}) and the standard conversion (Kennicutt 1998, see their equation 1), assuming a Salpeter IMF and a negligible dust correction. The SFRs for LAE components range from $\sim 0.1 M_{\odot} \text{ yr}^{-1}$ to $\sim 5 M_{\odot} \text{ yr}^{-1}$. The sum of SFRs in individual components is within 10 – 20% of the SFR for the composite system (as inferred from V^{PHOT}) when $S/N \gtrsim 30$ for the system. This is consistent with the difference between the half-light radii determined with PHOT and SExtractor for single-component systems (see Figure 8). In addition, we find that 8/15 of the two-component objects have SFR ratios less than

3:1. Although this could be interpreted as evidence for major merger events between individual components, the high rate of contamination expected in two-component objects and the depth dependence of the component segregation make it difficult to determine which, if any, of these LAEs are ongoing major mergers.

Considering that LAEs are thought to have stellar masses of $M \sim 10^9 M_{\odot}$ (Gawiser et al. 2007), there is no local analog for this level of star formation activity in objects of comparable mass. However, the SFRs and sizes of LAE components ($\lesssim 1$ kpc) are comparable to those of the nuclei of M82-like starburst galaxies in the local universe (Mayya et al. 2004). At $z \sim 3$, galaxies identified using other selection techniques, such as LBGs and submillimeter galaxies, have typical star formation rates that are at least an order of magnitude larger than those in LAEs and their components (Shapley et al. 2001; Genzel et al. 2003). However, LBGs have also been shown to exhibit clumpy star formation (Papovich et al. 2005) and may be undergoing a dynamical process similar to that leading to the active star formation and line emission seen in LAEs. An application of the pipeline developed here to LBGs would help to elucidate this comparison.

Support for this work was provided by NASA through grant number HST-AR-11253.01-A from the Space Telescope Science Institute, which is operated by AURA, Inc., under NASA contract NAS 5-26555 and by the National Science Foundation under grant AST-0807570. C. Gronwall was provided support through grant number HST-AR-10324.01-A. We thank Peter Kurczynski for his helpful suggestions on the point source analysis.

REFERENCES

- Altmann, M., Méndez, R. A., van Altena, W., Korchagin, V., & Ruiz, M. T. 2006, in *Revista Mexicana de Astronomía y Astrofísica Conference Series*, Vol. 26, *Revista Mexicana de Astronomía y Astrofísica Conference Series*, 64–65
- Beckwith, S. V. W. et al. 2006, *AJ*, 132, 1729
- Bertin, E. & Arnouts, S. 1996, *A&AS*, 117, 393
- Bond, N. 2009, *New Astronomy Review*, 53, 42
- Conselice, C. J. 2003, *ApJS*, 147, 1
- Conselice, C. J., Blackburne, J. A., & Papovich, C. 2005, *ApJ*, 620, 564
- Conselice, C. J. et al. 2004, *ApJ*, 600, L139
- Cowie, L. L. & Hu, E. M. 1998, *AJ*, 115, 1319
- Dickinson, M. 2000, in *Royal Society of London Philosophical Transactions Series A*, Vol. 358, *Astronomy, physics and chemistry of H_3^+* , 2001–+
- Ferguson, H. C. et al. 2004, *ApJ*, 600, L107
- Finkelstein, S. L., Cohen, S. H., Malhotra, S., Rhoads, J. E., & Papovich, C. 2009, *ArXiv e-prints*
- Fynbo, J. U., Møller, P., & Warren, S. J. 1999, *MNRAS*, 305, 849
- Gawiser, E. et al. 2006, *ApJS*, 162, 1
- . 2007, *ApJ*, 671, 278
- Genzel, R., Baker, A. J., Tacconi, L. J., Lutz, D., Cox, P., Guilloteau, S., & Omont, A. 2003, *ApJ*, 584, 633
- Giavalisco, M. et al. 2004, *ApJ*, 600, L93
- Gronwall, C. et al. 2007, *ApJ*, 667, 79
- Kennicutt, Jr., R. C. 1998, *ARA&A*, 36, 189
- Koekemoer, A. M., Fruchter, A. S., Hook, R. N., & Hack, W. 2002, in *The 2002 HST Calibration Workshop : Hubble after the Installation of the ACS and the NICMOS Cooling System*, ed. S. Arribas, A. Koekemoer, & B. Whitmore, 337–+
- Kron, R. G. 1980, *ApJS*, 43, 305
- Lotz, J. M., Madau, P., Giavalisco, M., Primack, J., & Ferguson, H. C. 2006, *ApJ*, 636, 592
- Mayya, Y. D., Bressan, A., Rodríguez, M., Valdes, J. R., & Chavez, M. 2004, *ApJ*, 600, 188
- Nilsson, K. K. et al. 2009, *A&A*, 498, 13
- Ostlin, G., Hayes, M., Kunth, D., Mas-Hesse, J. M., Leitherer, C., Petrosian, A., & Atek, H. 2008, *ArXiv e-prints*
- Overzier, R. A. et al. 2008, *ApJ*, 673, 143
- Papovich, C., Dickinson, M., Giavalisco, M., Conselice, C. J., & Ferguson, H. C. 2005, *ApJ*, 631, 101
- Peng, C. Y., Ho, L. C., Impey, C. D., & Rix, H.-W. 2002, *AJ*, 124, 266
- Pirzkal, N., Malhotra, S., Rhoads, J. E., & Xu, C. 2007, *ApJ*, 667, 49
- Press, W. H., Teukolsky, S. A., Vetterling, W. T., & Flannery, B. P. 1992, *Numerical recipes in C. The art of scientific computing* (Cambridge: University Press, —c1992, 2nd ed.)
- Ravindranath, S. et al. 2006, *ApJ*, 652, 963
- Rix, H.-W. et al. 2004, *ApJS*, 152, 163
- Schechter, P. 1976, *ApJ*, 203, 297
- Sersic, J. L. 1968, *Atlas de galaxias australes* (Cordoba, Argentina: Observatorio Astronomico, 1968)
- Shapley, A. E., Steidel, C. C., Adelberger, K. L., Dickinson, M., Giavalisco, M., & Pettini, M. 2001, *ApJ*, 562, 95
- Spergel, D. N. et al. 2007, *ApJS*, 170, 377
- Steidel, C. C., Adelberger, K. L., Shapley, A. E., Pettini, M., Dickinson, M., & Giavalisco, M. 2000, *ApJ*, 532, 170
- Steidel, C. C., Giavalisco, M., Dickinson, M., & Adelberger, K. L. 1996, *AJ*, 112, 352
- Taniguchi, Y. et al. 2009, *ArXiv e-prints*
- Venemans, B. P. et al. 2005, *A&A*, 431, 793

Yang, Y., Zabludoff, A., Tremonti, C., Eisenstein,
D., & Davé, R. 2009, ApJ, 693, 1579

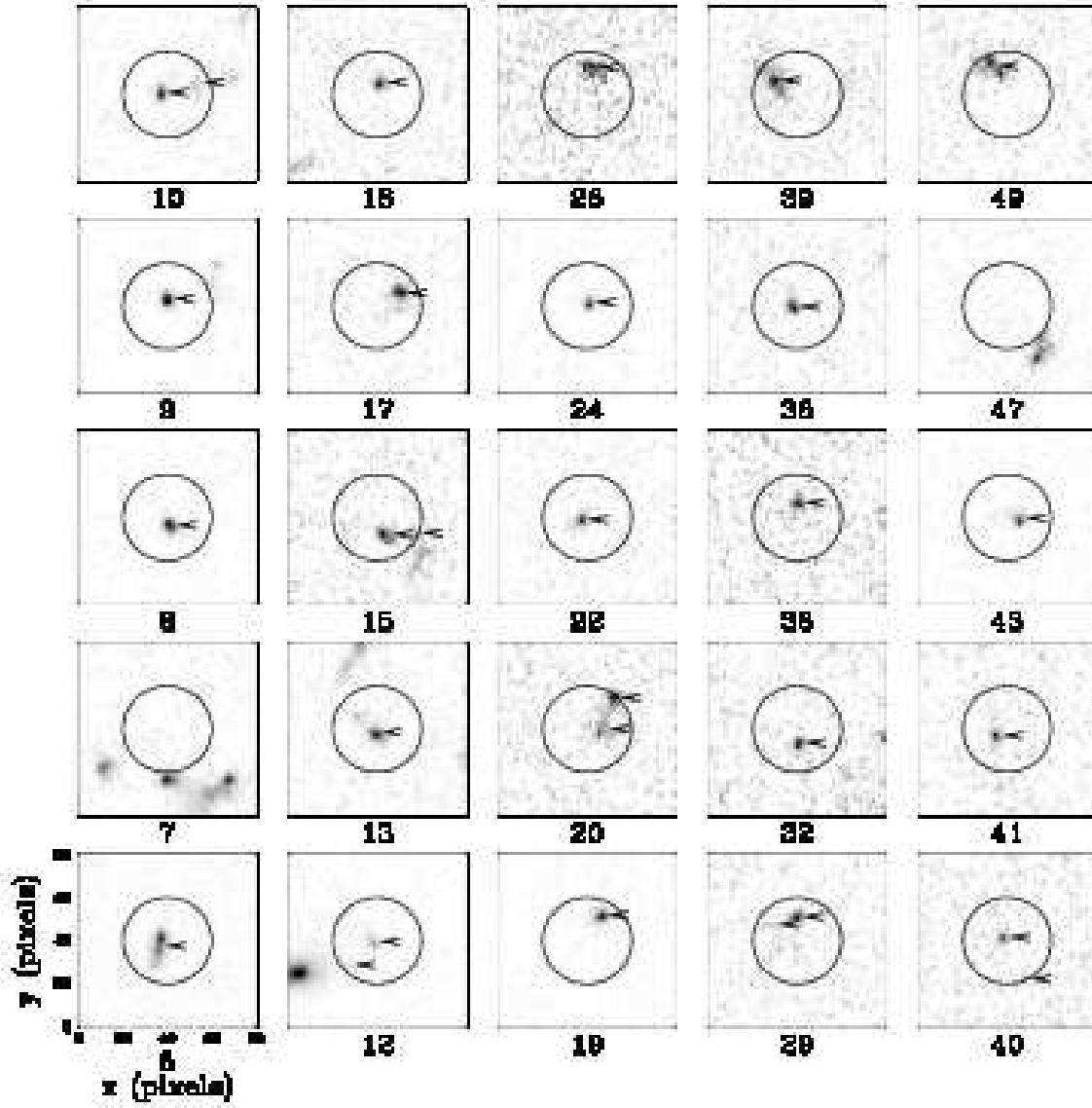


Fig. 10.— LAE cutouts extracted from the GEMS survey images. We mark components with red arrows and draw the selection circle in black. Numbers underneath the panels are the corresponding LAE indices from Gronwall et al. (2007).

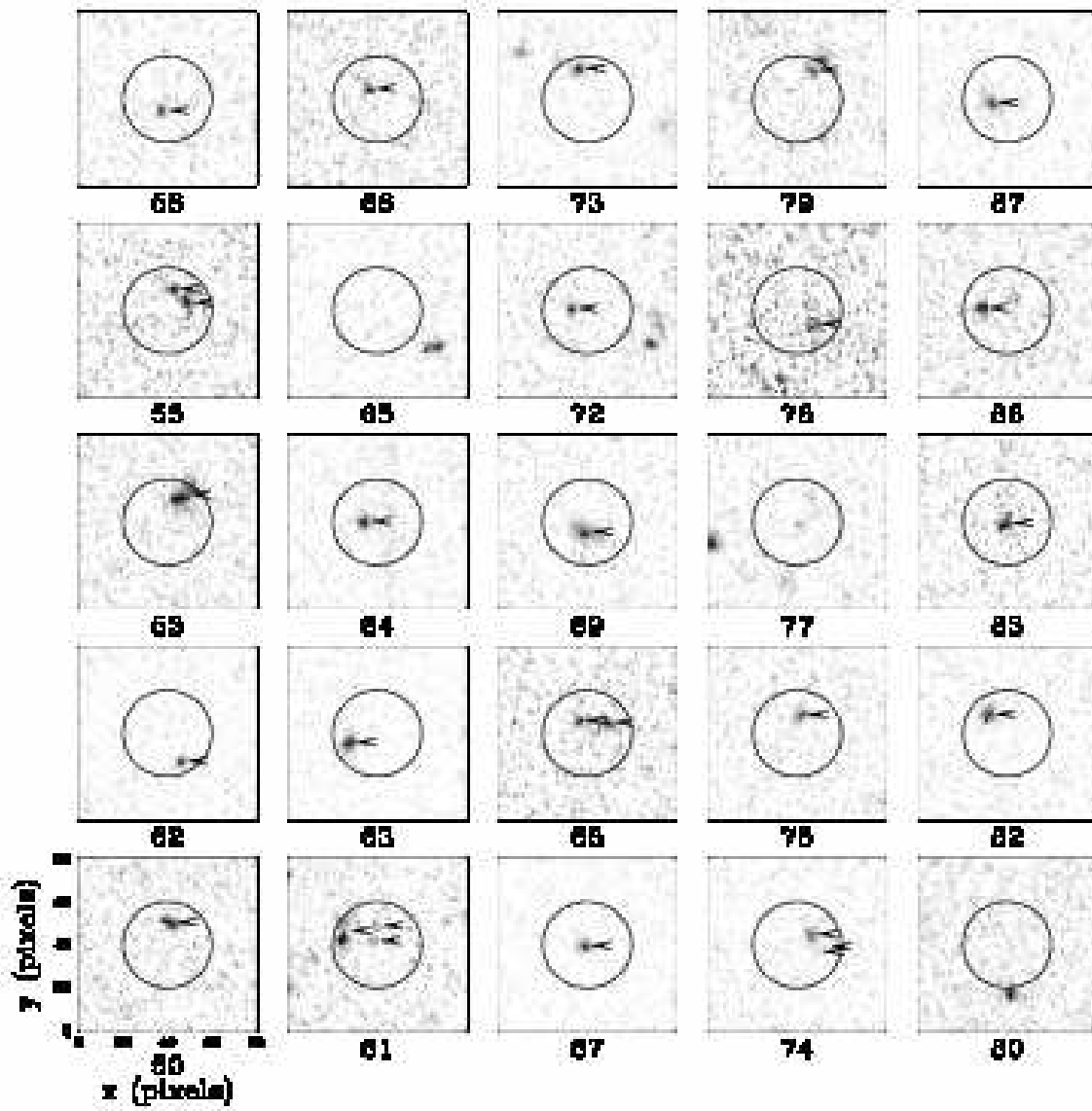


Fig. 10.— (cont.)

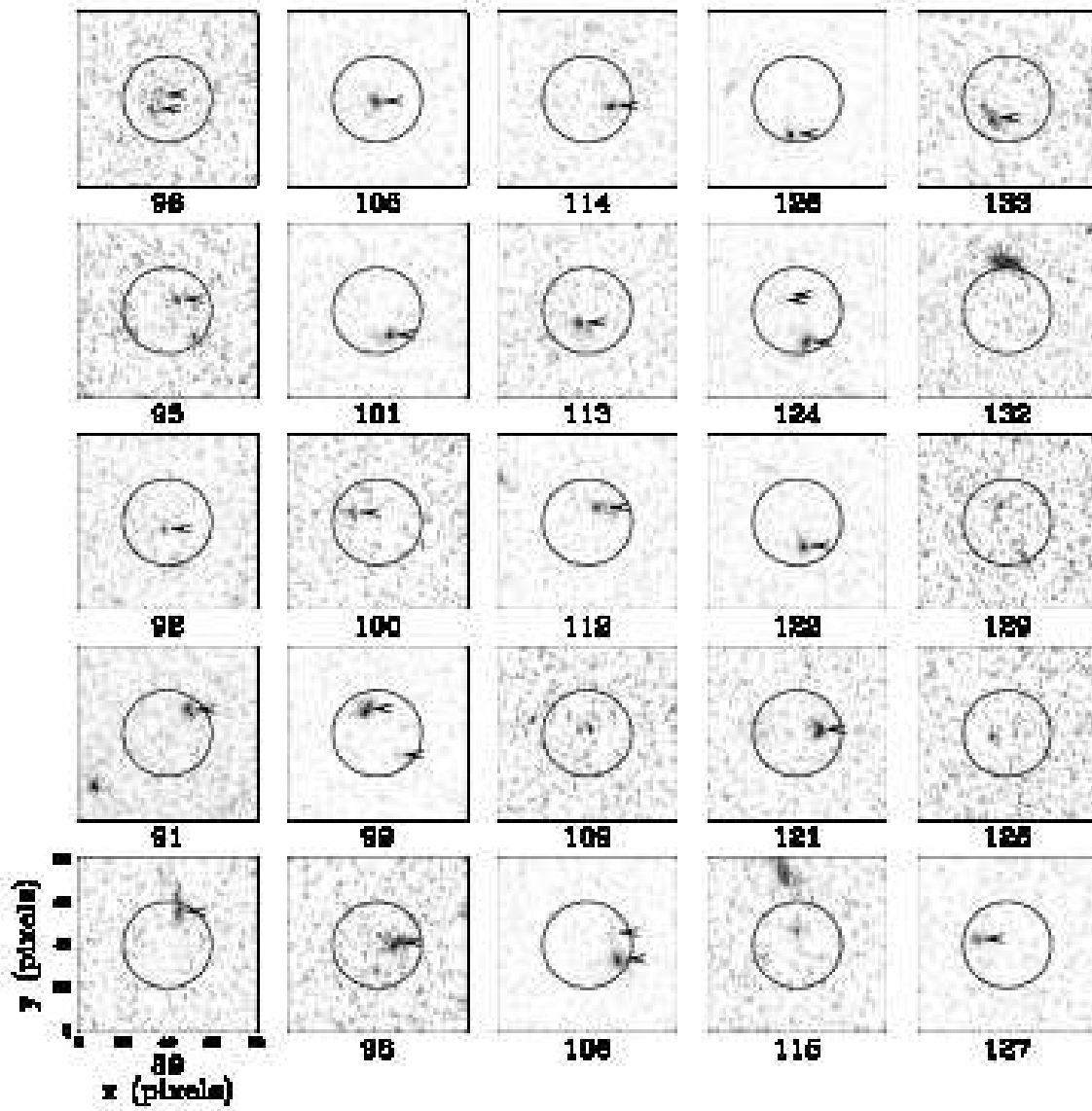


Fig. 10.— (cont.)

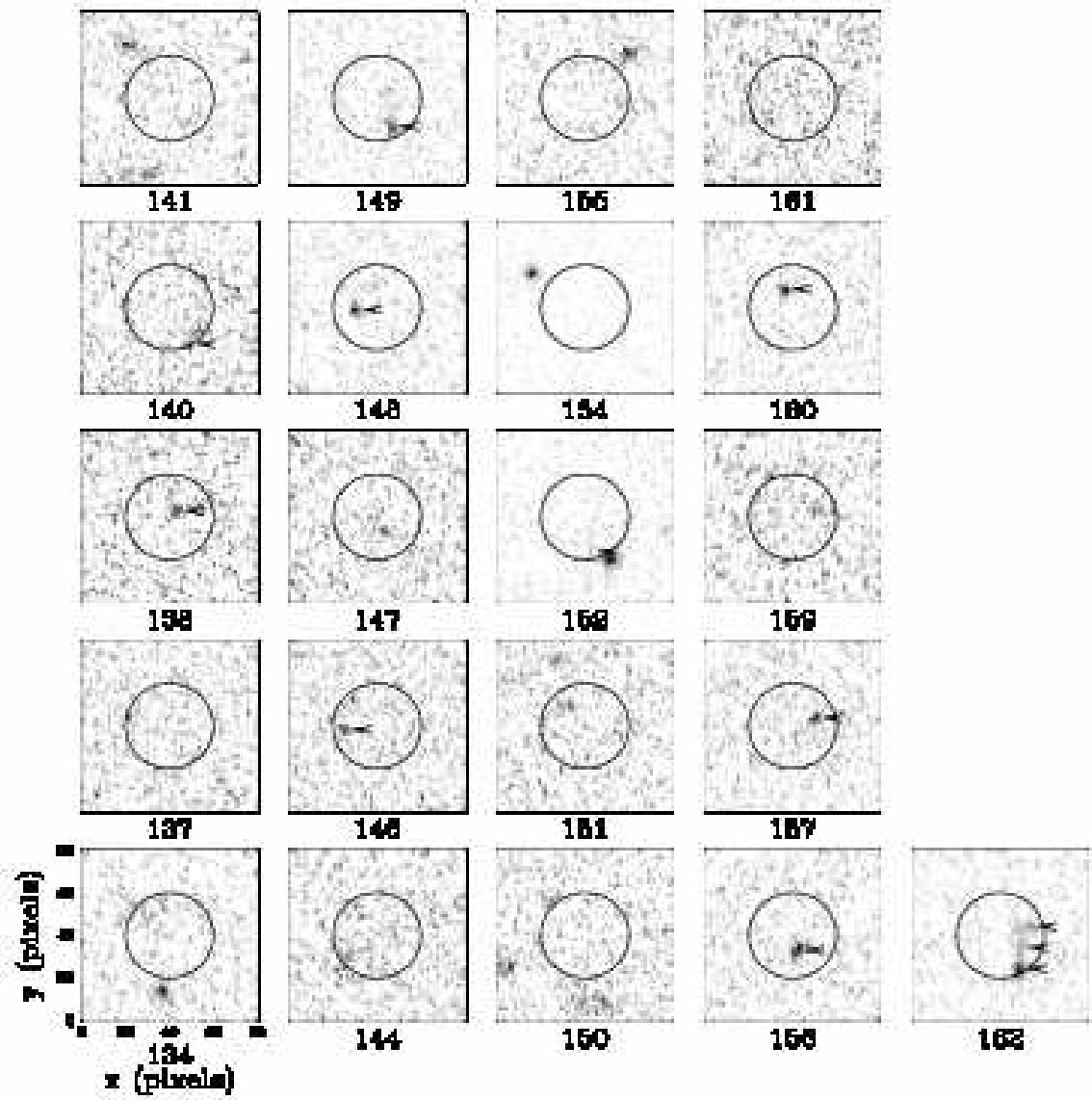


Fig. 10.— (cont.)

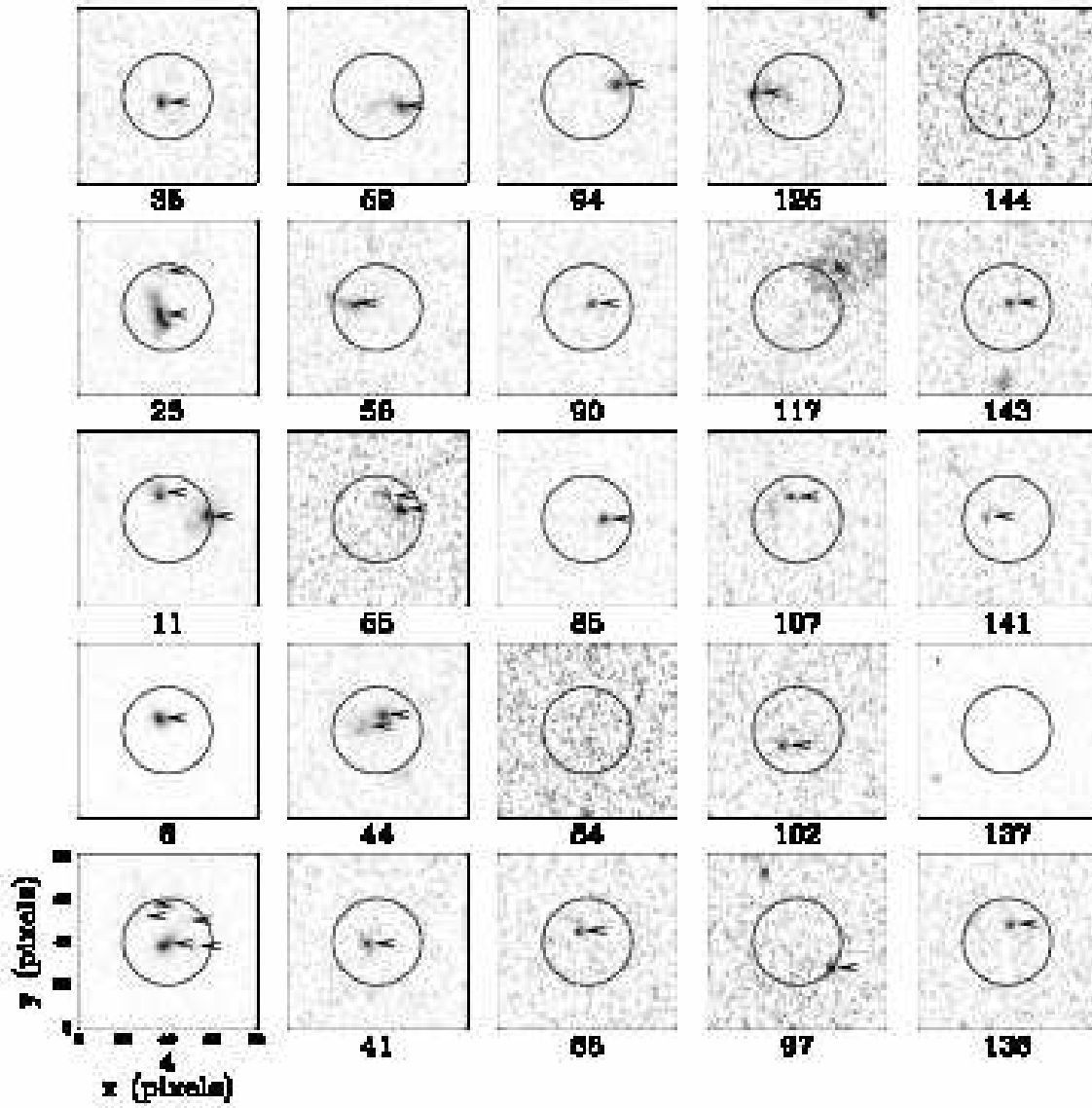


Fig. 11.— Same as Figure 10, but for LAEs detected in the GOODS survey.

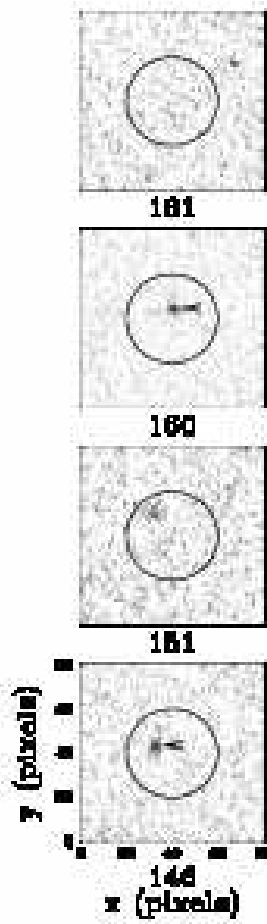


Fig. 11.— (cont.)

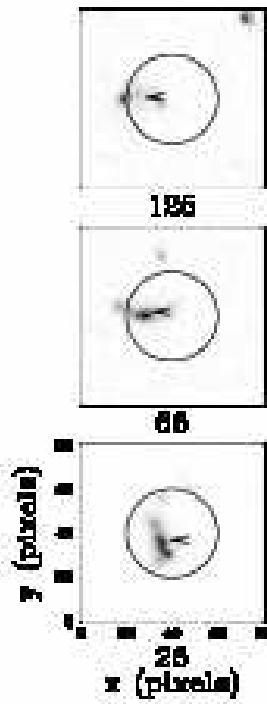


Fig. 12.— Same as Figure 10, but for LAEs detected in the HUDF survey.

TABLE 2
LAE PHOTOMETRIC PROPERTIES IN GEMS

Number ^a	Survey	α^b	δ^b	V^{PHOT} (AB mags)	d_c^c (")	$r_e^{\text{PHOT} d}$ (")
25	HUDF	3:32:40.785	-27:46:06.037	25.04 ± 0.01	0.19	0.19
56	HUDF	3:32:34.328	-27:47:59.545	26.30 ± 0.02	0.43	0.18
125	HUDF	3:32:39.013	-27:46:22.311	26.47 ± 0.02	0.53	0.22
4	GOODS	3:32:18.813	-27:42:48.103	24.89 ± 0.03	0.36	0.19
6	GOODS	3:32:52.690	-27:48:09.284	25.38 ± 0.03	0.19	0.09
11	GOODS	3:32:26.937	-27:41:27.937	25.16 ± 0.03	0.33	0.33
25	GOODS	3:32:40.785	-27:46:05.997	25.04 ± 0.03	0.16	0.20
35	GOODS	3:32:45.604	-27:52:10.914	26.81 ± 0.11	0.16	0.11
41	GOODS	3:32:56.672	-27:49:49.199	26.78 ± 0.20	0.19	0.09
44	GOODS	3:32:15.799	-27:44:09.993	26.01 ± 0.05	0.45	0.20
55	GOODS	3:32:59.976	-27:50:26.308	26.37 ± 0.18	0.31	0.17
56	GOODS	3:32:34.331	-27:47:59.554	26.44 ± 0.11	0.46	0.19
59	GOODS	3:32:33.254	-27:51:27.590	25.86 ± 0.06	0.32	0.17
66	GOODS	3:32:48.528	-27:56:05.376	26.66 ± 0.20	0.19	0.25
84	GOODS	3:32:17.395	-27:42:48.440	29.07 ± 1.20
85	GOODS	3:32:59.824	-27:53:05.768	26.62 ± 0.13	0.23	0.10
90	GOODS	3:32:14.574	-27:45:52.417	26.90 ± 0.16	0.30	0.12
94	GOODS	3:32:09.336	-27:43:54.193	26.63 ± 0.13	0.40	0.09
97	GOODS	3:32:12.584	-27:48:05.665	27.30 ± 0.21	0.63	0.16
102	GOODS	3:32:57.356	-27:51:42.357	27.38 ± 0.29	0.34	0.12
107	GOODS	3:32:10.158	-27:44:28.336	27.48 ± 0.28	0.60	0.15
117	GOODS	3:32:12.983	-27:44:52.140	27.77 ± 0.35
125	GOODS	3:32:39.016	-27:46:22.305	26.32 ± 0.09	0.58	0.20
136	GOODS	3:32:24.329	-27:41:51.886	27.32 ± 0.21	0.47	0.14
137	GOODS	3:32:59.951	-27:50:29.180	27.63 ± 0.56
141	GOODS	3:33:02.097	-27:51:07.663	27.45 ± 0.47	0.34	0.07
143	GOODS	3:32:54.652	-27:51:49.228	27.79 ± 0.39	0.03	0.08
144	GOODS	3:32:47.581	-27:55:38.250	28.67 ± 1.27
146	GOODS	3:32:44.168	-27:50:56.842	28.75 ± 0.88	0.27	0.04
151	GOODS	3:32:49.749	-27:46:43.793	28.95 ± 1.26	0.38	0.04
160	GOODS	3:32:02.802	-27:45:28.708	27.41 ± 0.22	0.39	0.09
161	GOODS	3:33:02.969	-27:50:29.420	28.51 ± 1.32
5	GEMS	3:32:47.516	-27:58:07.706	24.95 ± 0.03	0.18	0.15
7	GEMS	3:31:44.988	-27:35:32.870	27.45 ± 0.32
8	GEMS	3:31:54.885	-27:51:21.114	25.32 ± 0.04	0.14	0.09
9	GEMS	3:31:40.157	-28:03:07.406	25.06 ± 0.03	0.08	0.08
10	GEMS	3:33:22.442	-27:46:36.850	25.12 ± 0.04	0.19	0.28
12	GEMS	3:32:33.846	-27:36:35.117	25.26 ± 0.04	0.25	0.30
13	GEMS	3:33:07.252	-27:47:47.176	25.72 ± 0.07	0.09	0.11
15	GEMS	3:33:18.915	-27:38:28.469	25.75 ± 0.07	0.35	0.26

TABLE 2—*Continued*

Number ^a	Survey	α^b	δ^b	V^{PHOT} (AB mags)	d_c^c (")	r_e^{PHOT} ^d (")
17	GEMS	3:32:49.148	-27:34:39.971	25.55 ± 0.06	0.37	0.13
18	GEMS	3:32:46.754	-27:39:59.914	26.72 ± 0.16	0.15	0.08
19	GEMS	3:31:34.738	-27:56:21.821	25.08 ± 0.04	0.38	0.10
20	GEMS	3:33:11.879	-28:00:12.377	25.82 ± 0.07	0.35	0.25
22	GEMS	3:31:51.636	-27:58:32.642	26.18 ± 0.10	0.12	0.10
24	GEMS	3:31:53.213	-27:57:08.160	26.18 ± 0.09	0.03	0.08
26	GEMS	3:31:51.561	-27:46:47.016	26.16 ± 0.10	0.35	0.15
29	GEMS	3:31:47.800	-27:45:03.384	26.35 ± 0.12	0.25	0.16
32	GEMS	3:33:19.793	-27:38:20.505	27.25 ± 0.26	0.22	0.07
36	GEMS	3:32:18.926	-27:38:40.195	26.98 ± 0.21	0.18	0.10
38	GEMS	3:31:50.369	-27:59:10.119	26.52 ± 0.13	0.07	0.08
39	GEMS	3:31:30.524	-27:47:29.647	25.33 ± 0.04	0.40	0.20
40	GEMS	3:31:31.471	-27:34:47.404	27.19 ± 0.26	0.12	0.19
41	GEMS	3:32:56.672	-27:49:49.241	26.55 ± 0.14	0.21	0.12
43	GEMS	3:33:07.315	-27:54:38.983	25.78 ± 0.07	0.17	0.10
47	GEMS	3:32:43.499	-27:38:08.880	27.13 ± 0.25
49	GEMS	3:31:42.359	-27:58:07.857	25.69 ± 0.06	0.44	0.16
50	GEMS	3:31:52.830	-27:45:18.650	27.18 ± 0.24	0.28	0.08
52	GEMS	3:33:21.363	-27:38:36.337	26.91 ± 0.19	0.45	0.07
53	GEMS	3:32:15.131	-27:38:53.946	25.82 ± 0.07	0.42	0.16
55	GEMS	3:32:59.982	-27:50:26.367	26.37 ± 0.12	0.21	0.21
58	GEMS	3:33:06.943	-27:42:27.852	26.61 ± 0.14	0.21	0.13
61	GEMS	3:33:09.421	-27:45:50.114	26.09 ± 0.07	0.38	0.23
63	GEMS	3:32:51.917	-27:42:12.246	25.66 ± 0.06	0.47	0.10
64	GEMS	3:31:59.831	-27:49:46.424	25.99 ± 0.08	0.19	0.15
65	GEMS	3:31:42.733	-27:53:05.433	28.47 ± 0.81	0.41	0.34
66	GEMS	3:32:48.527	-27:56:05.357	27.80 ± 0.43	0.19	0.06
67	GEMS	3:32:51.770	-27:37:33.552	26.45 ± 0.12	0.04	0.07
68	GEMS	3:32:58.140	-27:48:04.877	26.70 ± 0.16	0.22	0.17
69	GEMS	3:33:25.357	-28:02:46.531	26.12 ± 0.09	0.16	0.13
72	GEMS	3:33:07.179	-27:48:51.544	27.00 ± 0.21	0.25	0.12
73	GEMS	3:32:57.404	-27:55:19.073	26.31 ± 0.11	0.41	0.11
74	GEMS	3:33:18.588	-27:45:42.617	26.67 ± 0.13	0.24	0.10
75	GEMS	3:32:59.268	-27:41:14.756	26.87 ± 0.19	0.24	0.10
77	GEMS	3:31:54.678	-27:52:52.927	27.75 ± 0.42	0.06	0.11
78	GEMS	3:33:20.840	-27:51:45.883	27.58 ± 0.35	0.32	0.10
79	GEMS	3:31:58.027	-27:47:30.335	26.26 ± 0.09	0.41	0.22
80	GEMS	3:33:20.491	-27:36:40.140	28.87 ± 1.21
82	GEMS	3:31:47.776	-27:42:16.325	26.43 ± 0.12	0.37	0.09
83	GEMS	3:31:38.670	-27:45:43.587	26.52 ± 0.11	0.08	0.12

TABLE 2—*Continued*

Number ^a	Survey	α^b	δ^b	V^{PHOT} (AB mags)	d_c^c (")	r_e^{PHOT} ^d (")
86	GEMS	3:33:28.159	-28:03:20.770	27.27 ± 0.27	0.24	0.19
87	GEMS	3:33:05.027	-27:43:37.306	25.98 ± 0.08	0.24	0.16
89	GEMS	3:33:12.017	-27:58:39.929	26.66 ± 0.16	0.45	0.18
91	GEMS	3:31:58.803	-27:49:28.767	26.91 ± 0.19	0.44	0.08
92	GEMS	3:33:03.319	-27:41:39.037	26.98 ± 0.21	0.33	0.30
95	GEMS	3:31:49.985	-27:51:39.640	27.48 ± 0.32	0.23	0.22
96	GEMS	3:31:48.355	-27:58:47.325	27.24 ± 0.21	0.19	0.14
98	GEMS	3:31:26.621	-27:44:02.180	26.55 ± 0.14	0.25	0.16
99	GEMS	3:31:40.241	-27:45:26.825	25.78 ± 0.07	0.22	0.18
100	GEMS	3:31:54.279	-27:58:03.475	27.55 ± 0.35	0.39	0.12
101	GEMS	3:33:07.750	-27:38:19.356	26.61 ± 0.15	0.40	0.11
105	GEMS	3:33:12.402	-27:45:24.309	26.28 ± 0.11	0.08	0.10
106	GEMS	3:32:21.285	-27:36:21.341	25.62 ± 0.06	0.46	0.17
109	GEMS	3:32:08.599	-27:57:11.897	28.98 ± 1.25	0.03	0.04
112	GEMS	3:32:44.073	-27:37:17.813	26.41 ± 0.12	0.27	0.12
113	GEMS	3:31:35.944	-27:50:52.915	26.57 ± 0.14	0.24	0.23
114	GEMS	3:32:10.528	-27:59:17.638	27.32 ± 0.28	0.37	0.07
115	GEMS	3:32:24.663	-28:01:53.101	28.70 ± 1.00	0.17	0.12
121	GEMS	3:33:23.709	-27:44:09.139	26.97 ± 0.21	0.31	0.09
122	GEMS	3:32:20.465	-27:35:01.627	26.48 ± 0.13	0.37	0.10
124	GEMS	3:31:42.925	-28:03:07.798	26.01 ± 0.08	0.42	0.16
126	GEMS	3:31:44.373	-27:50:57.703	26.29 ± 0.11	0.52	0.12
127	GEMS	3:33:02.820	-27:57:17.505	26.94 ± 0.20	0.45	0.10
128	GEMS	3:32:30.616	-28:00:47.901	0.25	...
129	GEMS	3:33:15.707	-28:02:19.075	28.66 ± 0.95	0.05	0.24
132	GEMS	3:32:10.122	-27:53:03.530
133	GEMS	3:31:42.953	-27:45:06.566	27.12 ± 0.23	0.36	0.12
134	GEMS	3:31:31.591	-27:47:07.650	27.43 ± 0.31
137	GEMS	3:32:59.993	-27:50:29.076	28.81 ± 1.09	0.64	0.05
138	GEMS	3:32:54.646	-27:38:54.076	27.40 ± 0.30	0.14	0.18
140	GEMS	3:33:24.452	-27:44:34.000	27.01 ± 0.22	0.63	0.28
141	GEMS	3:33:02.074	-27:51:07.660	28.66 ± 0.98
144	GEMS	3:32:47.581	-27:55:38.250	27.26 ± 0.26
145	GEMS	3:32:21.539	-27:36:04.378	27.29 ± 0.27	0.49	0.21
147	GEMS	3:31:44.967	-27:58:28.444	28.45 ± 0.81	0.24	0.07
148	GEMS	3:32:42.738	-27:39:39.981	27.53 ± 0.34	0.34	0.07
149	GEMS	3:33:07.027	-27:37:53.512	26.37 ± 0.12	0.48	0.16
150	GEMS	3:33:16.894	-27:43:53.100
151	GEMS	3:32:49.745	-27:46:43.785	28.30 ± 0.68	0.34	0.09
152	GEMS	3:33:29.304	-27:36:41.782	25.93 ± 0.08	0.52	0.29

TABLE 2—*Continued*

Number ^a	Survey	α^b	δ^b	V^{PHOT} (AB mags)	d_c^c (")	r_e^{PHOT} ^d (")
154	GEMS	3:31:53.538	-27:47:00.030	28.45 ± 0.78
155	GEMS	3:32:22.267	-27:34:58.630	28.36 ± 0.74
156	GEMS	3:33:00.604	-28:00:06.537	26.88 ± 0.18	0.25	0.11
157	GEMS	3:33:28.389	-27:45:09.634	26.84 ± 0.19	0.35	0.22
159	GEMS	3:31:29.732	-27:50:10.500	27.32 ± 0.27
160	GEMS	3:32:02.796	-27:45:28.796	27.65 ± 0.39	0.27	0.06
161	GEMS	3:33:02.969	-27:50:29.420	27.44 ± 0.31
162	GEMS	3:33:15.184	-27:54:01.642	25.74 ± 0.07	0.44	0.30

^aIndex from table 2 of Gronwall et al. 2007

^bPosition of ACS centroid (set to ground-based position when there are no SExtractor detections)

^cDistance between ACS and ground-based centroids

^dHalf-light radius computed by PHOT (not reported for LAEs without SExtractor detections)

TABLE 3
LAE COMPONENT PHOTOMETRIC PROPERTIES

Number ^a	Component ^b	Survey	α	δ	V^{SE}	d_c^c (")	b/a^d (AB mags)	θ^e ($^\circ$)	$r_e^{\text{SE} f}$ (")	SFR(UV) (M_\odot/yr)
25	1	HUDF	3:32:40.785	-27:46:06.037	25.04 ± 0.00	0.14	0.44	-80.30	0.19	4.27
56	1	HUDF	3:32:34.328	-27:47:59.545	26.37 ± 0.01	0.35	0.41	-4.20	0.17	1.26
125	1	HUDF	3:32:39.013	-27:46:22.311	26.56 ± 0.02	0.44	0.55	-1.20	0.21	1.06
4	1	GOODS	3:32:18.814	-27:42:48.194	25.27 ± 0.02	0.02	0.72	48.70	0.11	3.45
	2	GOODS	3:32:18.786	-27:42:48.226	27.48 ± 0.11	0.38	0.76	84.50	0.09	0.45
	3	GOODS	3:32:18.795	-27:42:47.868	27.56 ± 0.13	0.40	0.46	18.60	0.12	0.42
	4	GOODS	3:32:18.841	-27:42:47.809	27.62 ± 0.12	0.50	0.44	-77.50	0.12	0.40
	5	GOODS	3:32:18.835	-27:42:47.646	27.96 ± 0.12	0.59	0.19	-78.60	0.11	0.29
6	1	GOODS	3:32:52.690	-27:48:09.284	25.44 ± 0.02	0.19	0.83	-42.10	0.09	2.97
11	1	GOODS	3:32:26.922	-27:41:28.046	25.59 ± 0.03	0.54	0.72	53.80	0.17	2.59
	2	GOODS	3:32:26.969	-27:41:27.718	26.35 ± 0.04	0.38	0.90	-65.90	0.10	1.28
25	1	GOODS	3:32:40.785	-27:46:06.053	25.14 ± 0.02	0.12	0.42	-74.60	0.17	3.91
	2	GOODS	3:32:40.784	-27:46:05.450	27.63 ± 0.13	0.52	0.74	49.90	0.12	0.40
35	1	GOODS	3:32:45.604	-27:52:10.914	27.07 ± 0.06	0.09	0.88	87.50	0.08	0.66
41	1	GOODS	3:32:56.672	-27:49:49.199	26.83 ± 0.08	0.11	0.52	-62.10	0.08	0.82
44	1	GOODS	3:32:15.790	-27:44:09.919	26.51 ± 0.05	0.24	0.95	-25.50	0.13	1.11
	2	GOODS	3:32:15.809	-27:44:10.074	26.59 ± 0.07	0.16	0.71	28.60	0.19	1.03
55	1	GOODS	3:32:59.972	-27:50:26.366	26.88 ± 0.12	0.37	0.74	-18.60	0.09	0.79
	2	GOODS	3:32:59.985	-27:50:26.190	27.63 ± 0.19	0.36	0.47	-49.80	0.09	0.39
56	1	GOODS	3:32:34.331	-27:47:59.554	26.53 ± 0.08	0.37	0.29	-16.10	0.17	1.09
59	1	GOODS	3:32:33.254	-27:51:27.590	25.94 ± 0.05	0.31	0.46	-5.20	0.16	1.86
66	1	GOODS	3:32:48.528	-27:56:05.376	27.53 ± 0.15	0.18	0.79	17.90	0.07	0.43
85	1	GOODS	3:32:59.824	-27:53:05.768	26.98 ± 0.07	0.25	0.91	3.90	0.07	0.72
90	1	GOODS	3:32:14.574	-27:45:52.417	27.47 ± 0.08	0.10	0.73	38.20	0.06	0.46
94	1	GOODS	3:32:09.336	-27:43:54.193	26.72 ± 0.05	0.46	0.89	38.20	0.09	0.91
97	1	GOODS	3:32:12.584	-27:48:05.665	27.91 ± 0.13	0.60	0.77	-76.80	0.08	0.30
102	1	GOODS	3:32:57.356	-27:51:42.357	27.85 ± 0.15	0.26	0.68	73.80	0.08	0.32
107	1	GOODS	3:32:10.158	-27:44:28.336	27.92 ± 0.14	0.32	0.44	-9.20	0.08	0.30
125	1	GOODS	3:32:39.023	-27:46:22.290	27.08 ± 0.09	0.56	0.73	52.60	0.10	0.65
136	1	GOODS	3:32:24.329	-27:41:51.886	27.90 ± 0.11	0.26	0.74	73.40	0.07	0.31

TABLE 3—*Continued*

Number ^a	Component ^b	Survey	α	δ	V^{SE}	d_c^c ($''$)	b/a^d (AB mags)	θ^e ($^\circ$)	$r_e^{\text{SE} f}$ ($''$)	SFR(UV) (M_\odot/yr)
141	1	GOODS	3:33:02.097	-27:51:07.663	27.73 ± 0.15	0.26	0.45	79.70	0.06	0.36
143	1	GOODS	3:32:54.652	-27:51:49.228	28.00 ± 0.13	0.09	0.72	27.10	0.07	0.28
146	1	GOODS	3:32:44.168	-27:50:56.842	28.01 ± 0.13	0.21	0.83	66.60	0.07	0.28
160	1	GOODS	3:32:02.802	-27:45:28.708	27.74 ± 0.11	0.15	0.71	-34.40	0.07	0.36
5	1	GEMS	3:32:47.516	-27:58:07.706	25.01 ± 0.02	0.11	0.43	77.60	0.14	4.39
8	1	GEMS	3:31:54.884	-27:51:21.124	25.45 ± 0.02	0.12	0.77	-53.80	0.08	2.93
9	1	GEMS	3:31:40.157	-28:03:07.406	25.24 ± 0.01	0.10	0.82	85.30	0.07	3.57
10	1	GEMS	3:33:22.460	-27:46:36.923	25.87 ± 0.03	0.06	0.74	81.90	0.08	1.99
	2	GEMS	3:33:22.424	-27:46:36.777	25.96 ± 0.07	0.45	0.41	83.60	0.22	1.83
12	1	GEMS	3:32:33.838	-27:36:35.223	26.05 ± 0.05	0.03	0.66	-68.60	0.11	1.69
	2	GEMS	3:32:33.863	-27:36:34.885	26.85 ± 0.09	0.50	0.75	-81.80	0.16	0.81
13	1	GEMS	3:33:07.252	-27:47:47.176	25.65 ± 0.04	0.04	0.39	-45.80	0.11	2.45
15	1	GEMS	3:33:18.925	-27:38:28.474	26.49 ± 0.07	0.27	0.74	-49.60	0.10	1.12
	2	GEMS	3:33:18.894	-27:38:28.456	27.37 ± 0.13	0.58	0.53	68.30	0.13	0.50
17	1	GEMS	3:32:49.148	-27:34:39.971	25.67 ± 0.04	0.38	0.74	-85.80	0.12	2.40
18	1	GEMS	3:32:46.754	-27:39:59.914	26.77 ± 0.06	0.18	0.92	-78.20	0.08	0.87
19	1	GEMS	3:31:34.738	-27:56:21.821	25.30 ± 0.02	0.41	0.93	18.40	0.08	3.38
20	1	GEMS	3:33:11.883	-28:00:12.572	26.47 ± 0.09	0.24	0.82	71.20	0.15	1.15
	2	GEMS	3:33:11.873	-28:00:12.142	26.67 ± 0.07	0.58	0.84	86.50	0.09	0.95
22	1	GEMS	3:31:51.636	-27:58:32.642	26.41 ± 0.04	0.06	0.70	41.80	0.08	1.21
24	1	GEMS	3:31:53.213	-27:57:08.160	26.29 ± 0.04	0.07	0.85	50.70	0.07	1.36
26	1	GEMS	3:31:51.561	-27:46:47.016	26.53 ± 0.08	0.38	0.66	-12.50	0.11	1.08
29	1	GEMS	3:31:47.796	-27:45:03.320	26.75 ± 0.07	0.34	0.89	47.90	0.09	0.88
	2	GEMS	3:31:47.821	-27:45:03.434	28.99 ± 0.26	0.39	0.52	-17.00	0.05	0.11
32	1	GEMS	3:33:19.793	-27:38:20.505	27.17 ± 0.08	0.19	0.77	58.70	0.08	0.60
36	1	GEMS	3:32:18.926	-27:38:40.195	27.11 ± 0.12	0.21	0.84	-63.20	0.09	0.64
38	1	GEMS	3:31:50.369	-27:59:10.119	26.55 ± 0.05	0.03	0.86	-59.00	0.08	1.07
39	1	GEMS	3:31:30.524	-27:47:29.647	25.45 ± 0.03	0.35	0.45	-54.10	0.18	2.93
40	1	GEMS	3:31:31.477	-27:34:47.266	27.66 ± 0.13	0.06	0.63	-43.30	0.07	0.39
	2	GEMS	3:31:31.454	-27:34:47.849	28.94 ± 0.25	0.59	0.40	41.80	0.05	0.12

TABLE 3—*Continued*

Number ^a	Component ^b	Survey	α	δ	V^{SE}	d_c^c ($''$)	b/a^d (AB mags)	θ^e ($^\circ$)	$r_e^{\text{SE} f}$ ($''$)	SFR(UV) (M_\odot/yr)
41	1	GEMS	3:32:56.672	-27:49:49.241	26.88 ± 0.08	0.15	0.72	-83.10	0.09	0.79
43	1	GEMS	3:33:07.315	-27:54:38.983	25.93 ± 0.04	0.19	0.92	-60.70	0.08	1.88
49	1	GEMS	3:31:42.359	-27:58:07.857	25.76 ± 0.05	0.44	0.57	-30.60	0.15	2.20
50	1	GEMS	3:31:52.830	-27:45:18.650	27.09 ± 0.07	0.33	0.51	-22.20	0.08	0.65
52	1	GEMS	3:33:21.363	-27:38:36.337	27.05 ± 0.07	0.43	0.82	52.00	0.06	0.67
53	1	GEMS	3:32:15.131	-27:38:53.946	25.87 ± 0.04	0.46	0.58	47.40	0.16	2.00
55	1	GEMS	3:32:59.974	-27:50:26.401	26.71 ± 0.11	0.31	0.54	-77.30	0.14	0.92
	2	GEMS	3:32:59.988	-27:50:26.204	27.61 ± 0.13	0.33	0.69	2.00	0.08	0.40
58	1	GEMS	3:33:06.943	-27:42:27.852	27.08 ± 0.09	0.16	0.71	81.30	0.08	0.66
61	1	GEMS	3:33:09.431	-27:45:50.096	26.40 ± 0.06	0.47	0.51	75.50	0.14	1.22
	2	GEMS	3:33:09.398	-27:45:50.025	28.04 ± 0.12	0.27	0.84	-77.60	0.08	0.27
	3	GEMS	3:33:09.402	-27:45:50.235	28.59 ± 0.14	0.06	0.60	-2.50	0.05	0.16
63	1	GEMS	3:32:51.917	-27:42:12.246	25.81 ± 0.03	0.38	0.64	67.60	0.09	2.10
64	1	GEMS	3:31:59.831	-27:49:46.424	26.41 ± 0.06	0.16	0.83	53.40	0.09	1.21
66	1	GEMS	3:32:48.527	-27:56:05.357	27.92 ± 0.15	0.18	0.73	-40.00	0.06	0.30
67	1	GEMS	3:32:51.770	-27:37:33.552	26.36 ± 0.04	0.02	0.91	0.80	0.08	1.27
68	1	GEMS	3:32:58.130	-27:48:04.885	27.20 ± 0.12	0.33	0.73	-42.00	0.10	0.59
	2	GEMS	3:32:58.159	-27:48:04.861	27.95 ± 0.15	0.20	0.63	45.20	0.07	0.29
69	1	GEMS	3:33:25.357	-28:02:46.531	26.11 ± 0.05	0.13	0.67	-23.80	0.13	1.60
72	1	GEMS	3:33:07.179	-27:48:51.544	27.41 ± 0.11	0.20	0.73	-55.30	0.07	0.48
73	1	GEMS	3:32:57.404	-27:55:19.073	26.59 ± 0.06	0.44	0.89	34.60	0.08	1.02
74	1	GEMS	3:33:18.589	-27:45:42.588	26.78 ± 0.05	0.26	0.83	80.30	0.08	0.86
	2	GEMS	3:33:18.575	-27:45:42.755	29.46 ± 0.42	0.39	0.63	47.50	0.05	0.07
	3	GEMS	3:33:18.584	-27:45:42.826	29.87 ± 0.46	0.30	0.52	-62.50	0.03	0.05
75	1	GEMS	3:32:59.268	-27:41:14.756	27.12 ± 0.09	0.27	0.56	37.20	0.08	0.63
78	1	GEMS	3:33:20.840	-27:51:45.883	27.54 ± 0.23	0.30	0.97	-42.40	0.11	0.43
79	1	GEMS	3:31:58.025	-27:47:30.314	27.14 ± 0.07	0.46	0.70	-45.20	0.08	0.62
82	1	GEMS	3:31:47.776	-27:42:16.325	26.39 ± 0.05	0.36	0.78	72.20	0.09	1.23
83	1	GEMS	3:31:38.669	-27:45:43.559	26.80 ± 0.06	0.01	0.81	72.90	0.10	0.84
86	1	GEMS	3:33:28.170	-28:03:20.782	27.47 ± 0.09	0.33	0.95	-34.80	0.07	0.46

TABLE 3—*Continued*

Number ^a	Component ^b	Survey	α	δ	V^{SE}	d_c^c ($''$)	b/a^d (AB mags)	θ^e ($^\circ$)	$r_e^{\text{SE} f}$ ($''$)	SFR(UV) (M_\odot/yr)
87	1	GEMS	3:33:05.027	-27:43:37.306	26.31 ± 0.06	0.20	0.56	-39.80	0.11	1.32
89	1	GEMS	3:33:12.017	-27:58:39.929	27.11 ± 0.12	0.49	0.38	87.50	0.11	0.64
91	1	GEMS	3:31:58.803	-27:49:28.767	26.85 ± 0.07	0.46	0.67	-68.80	0.09	0.81
92	1	GEMS	3:33:03.327	-27:41:38.828	28.31 ± 0.15	0.09	0.58	82.10	0.05	0.21
95	1	GEMS	3:31:49.991	-27:51:39.476	28.02 ± 0.18	0.22	0.59	54.00	0.08	0.28
96	1	GEMS	3:31:48.358	-27:58:47.429	27.51 ± 0.09	0.21	0.70	-69.10	0.10	0.44
	2	GEMS	3:31:48.352	-27:58:47.229	27.52 ± 0.13	0.11	0.79	46.50	0.12	0.44
98	1	GEMS	3:31:26.620	-27:44:02.186	26.85 ± 0.10	0.26	0.59	25.20	0.13	0.81
99	1	GEMS	3:31:40.247	-27:45:26.715	26.08 ± 0.04	0.38	0.69	44.00	0.10	1.64
	2	GEMS	3:31:40.214	-27:45:27.357	28.09 ± 0.20	0.41	0.55	-8.80	0.09	0.26
100	1	GEMS	3:31:54.279	-27:58:03.475	28.14 ± 0.19	0.34	0.43	-54.40	0.07	0.25
101	1	GEMS	3:33:07.750	-27:38:19.356	26.82 ± 0.09	0.37	0.57	19.70	0.09	0.83
105	1	GEMS	3:33:12.402	-27:45:24.309	26.31 ± 0.06	0.02	0.82	-71.00	0.10	1.33
106	1	GEMS	3:32:21.284	-27:36:21.415	25.86 ± 0.05	0.49	0.71	-51.60	0.12	2.01
	2	GEMS	3:32:21.291	-27:36:21.046	27.36 ± 0.15	0.39	0.54	79.00	0.14	0.51
112	1	GEMS	3:32:44.073	-27:37:17.813	26.44 ± 0.06	0.30	0.48	-14.50	0.12	1.18
113	1	GEMS	3:31:35.944	-27:50:52.915	27.36 ± 0.12	0.20	0.73	-80.50	0.09	0.51
114	1	GEMS	3:32:10.528	-27:59:17.638	27.17 ± 0.09	0.36	0.61	10.90	0.08	0.60
121	1	GEMS	3:33:23.709	-27:44:09.139	27.11 ± 0.10	0.32	0.56	-81.30	0.08	0.64
122	1	GEMS	3:32:20.465	-27:35:01.627	26.54 ± 0.06	0.34	0.61	-75.30	0.09	1.07
124	1	GEMS	3:31:42.923	-28:03:07.855	26.38 ± 0.06	0.45	0.51	59.00	0.10	1.25
	2	GEMS	3:31:42.949	-28:03:07.277	28.90 ± 0.31	0.26	0.48	-13.30	0.06	0.12
	3	GEMS	3:31:42.943	-28:03:07.203	29.57 ± 0.37	0.26	0.53	-42.90	0.07	0.07
126	1	GEMS	3:31:44.373	-27:50:57.703	26.59 ± 0.06	0.48	0.83	-59.10	0.08	1.03
127	1	GEMS	3:33:02.820	-27:57:17.505	27.17 ± 0.10	0.39	0.75	12.10	0.08	0.60
133	1	GEMS	3:31:42.953	-27:45:06.566	27.07 ± 0.12	0.31	0.50	-57.10	0.13	0.66
138	1	GEMS	3:32:54.646	-27:38:54.076	28.22 ± 0.23	0.16	0.40	53.20	0.07	0.23
140	1	GEMS	3:33:24.452	-27:44:34.000	28.24 ± 0.20	0.60	0.54	72.30	0.07	0.23
145	1	GEMS	3:32:21.541	-27:36:04.470	27.84 ± 0.18	0.42	0.59	-31.10	0.08	0.32
148	1	GEMS	3:32:42.738	-27:39:39.981	27.44 ± 0.08	0.27	0.74	-79.00	0.07	0.47

TABLE 3—*Continued*

Number ^a	Component ^b	Survey	α	δ	V^{SE}	d_c^c ($''$)	b/a^d (AB mags)	θ^e ($^\circ$)	$r_e^{\text{SE} f}$ ($''$)	SFR(UV) (M_\odot/yr)
149	1	GEMS	3:33:07.027	-27:37:53.512	26.81 ± 0.09	0.46	0.73	-82.00	0.10	0.84
152	1	GEMS	3:33:29.304	-27:36:41.782	27.91 ± 0.20	0.50	0.28	75.20	0.12	0.30
156	1	GEMS	3:33:00.604	-28:00:06.537	26.99 ± 0.09	0.22	0.58	66.60	0.10	0.71
157	1	GEMS	3:33:28.389	-27:45:09.634	27.47 ± 0.15	0.35	0.83	25.30	0.08	0.46
160	1	GEMS	3:32:02.796	-27:45:28.796	27.47 ± 0.11	0.28	0.63	-38.80	0.07	0.46
162	1	GEMS	3:33:15.187	-27:54:01.865	26.43 ± 0.07	0.55	0.72	71.70	0.11	1.19
	2	GEMS	3:33:15.185	-27:54:01.566	26.84 ± 0.09	0.35	0.58	77.60	0.18	0.82
	3	GEMS	3:33:15.176	-27:54:01.270	27.27 ± 0.13	0.44	0.58	1.50	0.12	0.55

^aIndex from table 2 of Gronwall et al. 2007

^bComponent number

^cDistance from ground-based Ly α position

^dIsophotal axis ratio computed by SExtractor

^eIsophotal position angle computed by SExtractor

^fHalf-light radius computed by SExtractor